

# The differences of baryonic and dark matter scaling relations in galaxy clusters between IllustrisTNG simulations and observations

Daniel Miller<sup>1</sup>, Diego Pallero<sup>2,3</sup>, Patricia B. Tissera<sup>4,5</sup>, Matías Blaña<sup>6</sup>

<sup>1</sup> Instituto de Física, Pontificia Universidad Católica de Valparaíso, Avenida Universidad 330, Curauma, Valparaíso, Chile, 2373223  
 e-mail: dmillerquintana@gmail.com, daniel.miller.q@mail.pucv.cl

<sup>2</sup> Departamento de Física, Universidad Federico Santa María, Avenida España 1680, Valparaíso, Chile, 2390123

<sup>3</sup> Millennium Nucleus for Galaxies (MINGAL)

<sup>4</sup> Instituto de Astrofísica, Pontificia Universidad Católica de Chile, Av. Vicuña Mackenna 4860, Santiago, Chile, 7820436

<sup>5</sup> Centro de Astro-Ingeniería, Pontificia Universidad Católica de Chile, Av. Vicuña Mackenna 4860, Santiago, Chile, 7820436

<sup>6</sup> Vicerrectoría de Investigación y Postgrado, Universidad de La Serena, La Serena, Chile, 1700000

Received 10 October 2024 / Accepted 17 April 2025

## ABSTRACT

We compare the self-similar baryonic mass fraction scaling relations between galaxy clusters from the South Pole Telescope Sunyaev-Zel'dovich (SPT-SZ) survey and the IllustrisTNG state-of-the-art magnetohydrodynamical cosmological simulations. Using samples of 218 (TNG100) and 1605 (TNG300) friends-of-friends (FoF) haloes within  $0.0 \leq z \leq 1.5$  and  $M_{200c} \geq 7 \times 10^{13} M_{\odot}$ , we fit the scaling relations using Simple Power Law (SPL), Broken Power Law (BPL), and General Double Power Law (GDPL) models through non-linear least squares regression. The SPL model reveals null slopes for the baryonic fraction as a function of redshift, consistent with self-similarity. Observations and simulations agree within  $1-2\sigma$ , suggesting comparable baryonic scaling slopes. We identify  $\sim 13.8-14.1$  per cent of baryons as "missing", primarily in the form of intracluster light (ICL) across all halo masses and warm gas in low-mass haloes. High-mass haloes ( $\log_{10}(M_{500c}/M_{\odot}) \geq 14$ ) adhere to self-similarity, while low-mass haloes exhibit deviations, with the breakpoint occurring at  $\log_{10}(M_{500c}/M_{\odot}) \sim 14$ , where baryons are redistributed to the outskirts. Our findings suggest that the undetected warm-hot intergalactic medium (WHIM) and baryon redistribution by feedback mechanisms are complementary solutions to the "missing baryon" problem.

**Key words.** Methods: Numerical — Galaxies: Clusters: General — Galaxies: Clusters: Intracluster medium — Cosmology: Theory — (Cosmology:) Dark matter — (Cosmology:) Large-scale structure of Universe

## 1. Introduction

One of the last century's key discoveries was that the Universe is expanding. Nowadays, we have a very well-constrained "standard model", called "Lambda Cold Dark Matter" ( $\Lambda$ CDM), which says that the Universe is composed of dark energy ( $\Omega_{\Lambda} \sim 0.69$ ) and matter ( $\Omega_m = \Omega_b + \Omega_{dm} \sim 0.31$ ), which  $\Omega_b$  represents the baryonic density and  $\Omega_{dm}$  the dark matter density. From the matter density, 15.7 per cent corresponds to baryons, while  $\sim 84.3$  per cent is attributed to dark matter (Planck Collaboration et al. 2016a). This predominance of dark matter over visible matter significantly impacts the gravitational processes driving the formation of structures; briefly, after the Big Bang, small quantum perturbations in the density field lead to matter overdensities. As Dark Matter only interacts gravitationally, it had time to clump up and grow, forming the first dark matter haloes. These regions started to grow by accreting baryons and smaller haloes (White & Rees 1978; White & Frenk 1991). Several authors have thoroughly reviewed this "hierarchical structure formation" scenario in the last decades through analytical studies (e.g. Press & Schechter 1974; White & Rees 1978; White & Frenk 1991) and numerical simulations (e.g. White 1978; Villumsen 1982; McGee et al. 2009; Pallero et al. 2019).

Within these haloes, galaxy clusters are a key piece in the puzzle to understand the evolution of the Universe, as they are the largest gravitationally bound structures. To form this kind

of structure, matter of large regions of the Universe should collapse ( $\sim 10$ Mpc); so they are expected to have a baryon fraction close to the universal value,  $f_{bar}^U \sim \Omega_b/\Omega_m \sim 0.157 \pm 0.004$  (Planck Collaboration et al. 2016a). Observational results indicate that massive clusters  $\log_{10}(M_{200c}/M_{\odot}) \gtrsim 14.5$  typically exhibit a baryonic fraction close to this universal value, as expected (Giodini et al. 2009). Furthermore, Sunyaev-Zel'dovich (SZ) surveys and X-ray measurements have confirmed similar results (Chiu et al. 2018, C18 hereafter). However, low-mass clusters and groups of galaxies do not fulfill these expectations (e.g. Ettori 2003; McGaugh et al. 2010; Lovisari, L. et al. 2015; Chiu et al. 2018).

The last point highlights a discrepancy between early-time observations of baryon fractions in the Cosmic Microwave Background (CMB) (e.g. Planck Collaboration et al. 2016a) and late-time Sunyaev-Zel'dovich (SZ) and X-ray observations of galaxy groups and clusters. For example, C18 analyzed the baryon fraction,  $f_{bar,500c} = f_{star,500c} + f_{hot-gas,500c}$ , of 91 self-similar clusters in the redshift range  $0.20 < z < 1.25$ , using data from the SPT-SZ survey and Chandra X-ray observations. By employing scaling relations for X-ray hot gas and galaxy stellar mass, they found that clusters with  $\log_{10}(M_{500c}/M_{\odot}) \gtrsim 14.9$  reach a baryon fraction close to the universal value. However, clusters with  $\log_{10}(M_{500c}/M_{\odot}) \lesssim 14.9$  exhibit significantly lower baryon fractions. These observations suggest that not all baryonic matter in low-mass clusters is detected, even though it should reside

within their halo boundaries (Shull et al. 2012; Sanderson et al. 2013). This discrepancy presents a key challenge in the  $\Lambda$ CDM model, commonly called the "missing baryon" problem. Additionally, C18 found that baryon fractions vary strongly with total mass but weakly with redshift. These two properties are inconsistent with a hierarchical scenario, such as the most massive clusters, with baryon fractions near the universal value, could not have formed through the accretion of low-mass clusters with lower baryon fractions.

Studies from cosmological simulations and observations led to two main explanations for the missing baryons. The first suggests the existence of warm-hot gas in the intergalactic medium (WHIM) at temperatures of  $10^5 - 10^7$  K (Cen & Ostriker 1999). Nicastro et al. (2018) detected diffuse WHIM using two OVII absorption line tracers, although their measurements involve considerable uncertainties, as the signals could originate from sources other than WHIM itself (Johnson et al. 2019). Additionally, de Graaff et al. (2019) detected WHIM through the Planck thermal Sunyaev-Zel'dovich (tSZ) signal (Planck Collaboration et al. 2016b), and WHIM has been characterized and analyzed in magnetohydrodynamical simulations (e.g. Martizzi et al. 2019). The second explanation posits that the missing baryons reside in regions outside the halo boundary, such as  $R_{500c}$  or  $R_{200c}$  (e.g. Haider et al. 2016; Ayromlou et al. 2021; Gouin et al. 2022; Ayromlou et al. 2023). Feedback processes redistribute baryons to the outskirts of the halo, particularly in haloes with  $\log_{10}(M_{200c}/M_{\odot}) \lesssim 14$  (Ayromlou et al. 2023, A23 hereafter). Using simulations, A23 introduced the closure radius,  $R_c$ , as the radius where the baryon fraction approaches the Universal value. For example, for haloes with  $\log_{10}(M_{200c}/M_{\odot}) \lesssim 14$ , AGN feedback processes redistribute baryons up to  $R_c \sim 1.5 - 2.5R_{200c}$  (Ayromlou et al. 2023). These two explanations are not mutually exclusive and provide complementary insights into galaxy evolution and large-scale structure cosmology (Walker et al. 2019; Nicastro et al. 2022).

The scaling relations are powerful tools for investigating the power laws associated with observables in haloes. The self-similar model (Kaiser 1986) provides a mathematical framework for describing scaling relations in hydrostatic equilibrium structures. These tools allow the connection of large samples of galaxy clusters to the measurement of cosmological parameters (Haiman et al. 2001; Holder et al. 2001; Carlstrom et al. 2002). Scaling relations have been extensively studied through X-ray observations (e.g. Mohr & Evrard 1997; Arnaud & Evrard 1999; Mohr et al. 1999; Reiprich & Böhringer 2002; O'Hara et al. 2006; Arnaud et al. 2007; Pratt et al. 2009; Sun et al. 2009; Vikhlinin et al. 2009; Mantz et al. 2016; Chiu et al. 2018) and hydrodynamical simulations (e.g. Evrard 1997; Bryan & Norman 1998; Nagai et al. 2007; Stanek et al. 2010; Pillepich et al. 2018; Pop et al. 2022a; Hadzhiyska et al. 2023a). The inclusion of AGN feedback processes in simulations significantly affects the X-ray and SZ scaling relations in galaxy groups (Puchwein et al. 2008; Fabjan et al. 2011; Pike et al. 2014; Planelles et al. 2013; Le Brun et al. 2016; Truong et al. 2017; Henden et al. 2018, 2019; Lim et al. 2021; Yang et al. 2022). Pop et al. (2022a, P22 hereafter) introduced a novel method for fitting a scaling relation using a General Double Power Law (GDPL), model derived from the broken power law (BPL: Jóhannesson et al. 2006) scheme. The GDPL model demonstrated superior performance in representing self-similarity for both relaxed and unrelaxed haloes at  $\log_{10}(M_{500c}/M_{\odot}) \gtrsim 14$  compared to the simple power law (SPL: Lotka 1926) in simulations. If the trends and slopes of the SPL scaling relations presented by C18 can be reproduced

in simulations, the missing baryons can be identified and further investigated.

In this work, we compare the self-similar scaling relations of galaxy clusters obtained from the observations of C18 with the hydrodynamical simulations. We use the suite of the cosmological magnetohydrodynamical simulations from the IllustrisTNG project, selecting a sample of haloes with  $M_{200c} \geq 7 \times 10^{13} M_{\odot}$  to match the observational mass conditions and scaling relations of C18. To study their behavior separately, cold and warm gas components are introduced into these scaling relations. We analyze the percentage distribution of the baryonic components of the haloes: cold gas, WHIM, hot gas, stellar mass from galaxies, and intracluster light (ICL). Finally, we fit the SPL, BPL, and GDPL models and examine their respective shapes.

This paper is structured as follows. In Section 2, we describe the methods used in this research, including simulations and observational data. Section 3 outlines the formalism of the baryonic self-similar scaling relations, incorporating both the SPL and GDPL approaches. In Section 4, we present the results of the SPL, BPL, and GDPL models for the baryonic fraction scaling relations, comparing these models with observational data, varying the galaxy aperture, and adding the remaining gas components. In Section 5, we discuss the implications of these results, particularly in the context of baryonic component accretion. Finally, in Section 6, we summarise our findings.

## 2. Simulations and observational data

### 2.1. IllustrisTNG: the state-of-art magneto-hydrodynamical and cosmological simulations

IllustrisTNG (Naiman et al. 2018, Nelson et al. 2018, Springel et al. 2018, Pillepich et al. 2018, Marinacci et al. 2018) is a comprehensive suite of state-of-the-art magnetohydrodynamical and cosmological simulations focused on the formation and evolution of galaxies. It uses the moving-mesh AREPO code (Springel 2010) to solve the Poisson's equations. Additionally, it solves magnetohydrodynamic equations using a Voronoi tessellation method (Pakmor et al. 2011; Pakmor & Springel 2013). It includes a physical model for galaxy formation, incorporating non-gravitational processes such as gas radiative cooling, star formation, stellar evolution, and stellar feedback (Pillepich et al. 2018). Additionally, IllustrisTNG accounts for the physics of supermassive black holes, including their seeding, merging, and feedback processes (Weinberger et al. 2017).

This work uses the TNG100 (~100 Mpc box size) and TNG300 (~300 Mpc box size) simulations. TNG100 offers a good compromise between a wide range of environments and resolution, while TNG300 provides the lowest resolution but allows for superior statistical analyses of galaxy clusters (see Table 1).

We define galaxy clusters as self-gravitating haloes with masses  $M_{200c} \geq 7 \times 10^{13} M_{\odot}$  (for any redshift), comparable to the mass of the Fornax cluster (Drinkwater et al. 2001). The haloes and subhaloes were identified in a two-step fashion. First, haloes were selected using the Friends-of-Friends algorithm (FoF: Davis & Djorgovski 1985; Springel et al. 2001), with a linking length of  $b = 0.2$ , applied only to dark matter particles. Then, subhaloes were selected within FoF haloes using the subfind algorithm (Springel et al. 2001; Dolag et al. 2009), as those self-gravitating structures residing within haloes. In this work, we define galaxies as those subhaloes which contain 1000 stellar particles, i.e.,  $M_{\text{star}} \geq 5 \times 10^9 M_{\odot}$  for TNG100 and  $M_{\text{star}} \geq 5 \times 10^{10} M_{\odot}$  for TNG300, to ensure enough reso-

**Table 1.** Parameters of TNG100 and TNG300 simulations from IllustrisTNG (Pillepich et al. 2018).

Simulation	$L_{\text{box}}$ (Mpc)	$N_{\text{gas}}$	$N_{\text{dm}}$	$m_{\text{bar}}$ ( $M_{\odot}$ )	$m_{\text{dm}}$ ( $M_{\odot}$ )
TNG100-1	110.7	$1820^3$	$1820^3$	$1.4 \times 10^6$	$7.5 \times 10^6$
TNG300-1	302.6	$2500^3$	$2500^3$	$1.1 \times 10^7$	$5.9 \times 10^7$

**Notes.** The parameters included are the box size ( $L_{\text{box}}$ ), the number of gas cells ( $N_{\text{gas}}$ ), the number of dark matter particles ( $N_{\text{dm}}$ ), the mean baryonic particle mass ( $m_{\text{bar}}$ ) and the mean dark matter particle mass ( $m_{\text{dm}}$ ).

**Table 2.** Mass notations.

Notation	Galaxy Aperture	$R_{500c}$	FoF
Dark matter mass in cluster	—	$M_{\text{dm},500c}$	$M_{\text{dm,FoF}}$
Hot-gas mass in cluster	—	$M_{\text{hot-gas},500c}$	$M_{\text{hot-gas,FoF}}$
Warm-gas mass in cluster	—	$M_{\text{warm-gas},500c}$	$M_{\text{warm-gas,FoF}}$
Cold-gas mass in cluster	—	$M_{\text{cold-gas},500c}$	$M_{\text{cold-gas,FoF}}$
Total gas mass in cluster	—	$M_{\text{gas},500c} \equiv \sum_{\psi} M_{\psi,500c}$	$M_{\text{gas,FoF}} \equiv \sum_{\psi} M_{\psi,\text{FoF}}$
Stellar Mass in cluster	—	$M_{\text{star},500c}$	$M_{\text{star,FoF}}$
Total mass of the cluster	—	$M_{500c}$	$M_{\text{FoF}}$
Sum of stellar mass in galaxies	$r_{\text{op}}$ subfind	$M_{\text{star},r_{\text{op}},500c}$ or $M_{\text{star},r_{\text{op}}}$ $M_{\text{star,subfind},500c}$ or $M_{\text{star,subfind}}$	$M_{\text{star},r_{\text{op}},\text{FoF}}$ or $M_{\text{star},r_{\text{op}}}$ $M_{\text{star,subfind},\text{FoF}}$ or $M_{\text{star,subfind}}$
Intra-cluster Light (ICL) mass	$r_{\text{op}}$ subfind	$M_{\text{ICL},r_{\text{op}},500c}$ or ICL ( $r_{\text{op}}$ ) $M_{\text{ICL,subfind},500c}$ or ICL (subfind)	$M_{\text{ICL},r_{\text{op}},\text{FoF}}$ $M_{\text{ICL,subfind},\text{FoF}}$

**Notes.** Mass notations for this study in  $R_{500c}$  and FoF. Includes the mass notations for the dark matter mass,  $\psi \in \{\text{hot-gas, warm-gas, cold-gas}\}$  gas components mass, total gas mass and stellar mass in the cluster, including the total mass notation. Also, includes the notation for the sum of stellar mass in galaxies depending of the galaxy aperture used. Finally, includes the definition and notation of Intra-cluster light (ICL) mass, as the cluster stellar mass minus the total stellar mass in the galaxies (depending of the galaxy aperture). The notations of  $M_{\text{star},r_{\text{op}}}$  and  $M_{\text{star,subfind}}$  are used in Fig. 1. The notations of ICL ( $r_{\text{op}}$ ) and ICL (subfind) are used in Table 3.

lution to avoid spurious identifications. Gas within structures is split into three components: cold gas ( $T < 10^5$  K), warm gas ( $10^5 \leq T < 10^7$  K), and hot gas ( $T \geq 10^7$  K) (Cen & Ostriker 1999; Martizzi et al. 2019; Gouin et al. 2022, 2023). The selection of these temperature thresholds stems from the fact that the star formation model in IllustrisTNG is based on an effective equation of state and a representation of cold and warm gas phases within each cell (Pillepich et al. 2018). Moreover, these thresholds are widely employed in IllustrisTNG studies to distinguish gas phases based on temperature and electron density (e.g. Martizzi et al. 2019; Gouin et al. 2022, 2023), as they effectively capture the gas phase diagram. Clusters were selected within  $0.0 \leq z \leq 1.5$ , with a time window between snapshots of 0.5 Gyr (TNG100) and 1.8 Gyr (TNG300). This resulted in a sample of 218 and 1605 clusters respectively.

For each cluster, we define a radius  $R_{\Delta} = R_{500c}$ , where the density is 500 times the critical density of the Universe (see Section 3). Then the baryon (gas and stars), the stellar, and the hot, warm and cold gas masses are all defined by adding the corresponding particles with  $R_{\Delta}$ . The total mass,  $M_{500c}$ , is the sum of  $M_{\text{bar},500c}$  and the dark matter mass,  $M_{\text{dm},500c}$ . Similarly, we use the cluster total mass, which is determined by the FoF algorithm. These masses are defined as  $M_{\text{bar,FoF}}$  for baryons,  $M_{\text{dm,FoF}}$  for dark matter, and  $M_{\text{FoF}} \equiv M_{\text{bar,FoF}} + M_{\text{dm,FoF}}$  for the total mass. The masses measured within  $R_{500c}$  are used to compare scaling relations in simulations with observations, while the FoF masses are employed to examine whether the self-similarity of the scaling relations is satisfied.

For galaxies in clusters, we define two apertures for mass measurement. The first corresponds to the subfind-measured masses of stars, gas (hot, warm, cold, or total), and dark matter. The second corresponds to a spherical aperture with a radius  $R_{\text{sph}} \equiv 2 \times R_{M_{\text{star}}/2}$ , comparable to the optical radius  $R_{\text{sph}} \sim r_{\text{op}}$ , which encloses most of the stellar flux in SED fitting (here, we

define  $R_{\text{sph}} \equiv r_{\text{op}}$  to present the results). This latter aperture is beneficial for comparing simulations with observations and to estimate the impact of systematic uncertainties in the scaling relations due to differences in the metrics to measure masses. Finally, we characterize the intracluster medium (ICM) as all the mass within the cluster that do not belong to galaxies according to our definitions. To summarize, Table 2 shows all the mass notations for the study.

## 2.2. Galaxy clusters in observations

To compare our results, we used the observations of C18, based on 91 galaxy clusters identified through the Sunyaev and Zeldovich effect (SZ) (Sunyaev & Zeldovich 1972) within the redshift range  $0.25 \leq z \leq 1.25$ . This sample was selected from the SPT-SZ survey (Bleem et al. 2015) and matched with Chandra X-ray observations. These measurements were further correlated with optical photometry in the griz bands from the Dark Energy Survey (DES; Dark Energy Survey Collaboration et al. 2016) and near-infrared photometry obtained using either the Wide-field Infrared Survey Explorer (WISE; Wright et al. 2010) or the Infrared Array Camera (IRAC; Fazio et al. 2004) aboard the Spitzer telescope.

C18 used the  $\zeta$ - $M_{500}$  scaling relations for the SZ-effect observable provided by the SPT collaboration, the  $\zeta$  normal distribution with the SZ-effect signal-to-noise ratio  $\xi$  as the unit width, and the calibrations from de Haan et al. (2016) to estimate the total mass  $M_{500c}$  for each cluster in the sample (based on Bocquet et al. 2015). The mass range of these clusters is  $M_{500c} = (2.63 - 12.71) \times 10^{14} M_{\odot}$ . The hot-gas mass,  $M_{\text{hot-gas},500c}$ , was determined using Chandra X-ray observations by fitting the best-fitting modified  $\beta$ -model (Vikhlinin et al. 2009) out to  $R_{500c}$  (based on McDonald et al. 2013). The stellar mass,  $M_{\text{star},500c}$ , was estimated by fitting the spectral energy distributions (SEDs) of



individual galaxies, constructing a stellar mass function (SMF; [Schechter 1976](#)), and summing the stellar masses of all galaxies in the cluster. Finally, the baryon fractions were calculated as the sum of the X-ray gas mass and the stellar mass of galaxies, normalized by  $M_{500c}$ . The baryon fractions for these clusters range from  $f_{\text{Chiu},500c} \approx 0.07 - 0.21$ .

### 3. Scaling relations

Most of this section is based on the mathematical developments of [Kaiser \(1986\)](#), [Mulroy et al. \(2019\)](#), and [P22](#). We follow their mathematical framework for the self-similar scaling relations of baryonic fractions in Subsection 3.1. Finally, the fitting procedures for the scaling relations are defined in Subsection 3.2.

#### 3.1. Self-similar model and baryonic mass fraction scaling relations

We assume that the hot gas is in hydrostatic equilibrium. Thus, we expect the pressure,  $P_{\text{gas}}$ , and the density,  $\rho_{\text{gas}}$ , of the gas to satisfy Eq. (1).

$$\frac{1}{\rho_{\text{gas}}} \frac{dP_{\text{gas}}}{dr} = -\frac{GM}{r^2} \quad (1)$$

The solution to the previous equation for the total mass, as a function of the gas density  $\rho_{\text{gas}}(r)$  and temperature  $T(r)$  profiles within the cluster, is given in Eq. (2).

$$M(< r) = -\frac{k_B r T(r)}{\mu m_p G} \left( \frac{d \ln \rho_{\text{gas}}(r)}{d \ln r} + \frac{d \ln T(r)}{d \ln r} \right) \quad (2)$$

If the mass is defined based on a spherical collapse model, the mass enclosed within a spherical region of radius  $R_\Delta$ , with  $\Delta$  times the critical density of the Universe  $\rho_c(z)$ , is given by Eq. (3).

$$M_\Delta = \frac{4\pi}{3} \Delta \rho_c(z) R_\Delta^3 \quad (3)$$

Eq. (4) defines the critical density of the Universe, where  $H(z) = H_0 E(z)$ , with  $H_0$  being the Hubble constant and  $E(z) \equiv \sqrt{\Omega_m (1+z)^3 + \Omega_\Lambda}$ .

$$\rho_c(z) = \frac{3H(z)^2}{8\pi G} \quad (4)$$

It is important to mention that the definitions of  $R_\Delta$  and  $M_\Delta$  depend on the overdensity value  $\Delta$ . In this study, we consider  $\Delta = \{500, 200\}$ .

In the self-similar model ([Kaiser 1986](#)), the properties of baryonic matter are scaled solely by the total cluster mass, independent of redshift. Thus,  $M_{\text{star},\Delta} \propto M_{\text{gas},\Delta} \propto M_{\text{star},\Delta} + M_{\text{gas},\Delta} = M_{\text{bar},\Delta} \propto M_\Delta$ . We define the fraction of a given baryonic component  $X$  (stellar, gas, or baryonic = stellar + gas) as shown in Eq. (5).

$$f_{X,\Delta} \equiv M_{X,\Delta}/M_\Delta \quad (5)$$

The scaling relation for these fractions is given in Eq. (6).

$$f_{\text{star},\Delta} \propto f_{\text{gas},\Delta} \propto f_{\text{bar},\Delta} \propto M_\Delta^0 = 1 \quad (6)$$

However, it is important to understand that the self-similarity model can be disrupted by non-gravitational processes such as gas cooling, stripping, winds, and feedback (both stellar and AGN) ([Kaiser 1986](#)).

#### 3.2. Fitting the power law to scaling relations

##### 3.2.1. Simple Power Law

The self-similarity model assumes that the scaling relations of galaxy clusters follow a simple power law (SPL: [Lotka 1926](#)) distribution ([Kaiser 1986](#)). If we have two observables,  $(X, Y)$ , the simple power law model relates them using two free parameters,  $(A_{\text{SPL}}, \alpha_{\text{SPL}})$ . Eq. (7) presents the simple power law model.

$$Y = A_{\text{SPL}} X^{\alpha_{\text{SPL}}} \quad (7)$$

##### 3.2.2. Broken Power Law and General Double Power Law

One of the findings from [P22](#) was that a simple power law is insufficient for describing the scaling relations in IllustrisTNG simulations. Feedback processes are more intense in low-mass haloes and groups of galaxies ([Ayromlou et al. 2021](#)), breaking the self-similarity of the scaling relations for these low-mass haloes. To address this, we use the General Double Power Law (GDPL) model. This model is based on the broken power law (BPL: [Jóhannesson et al. 2006](#)), where the data is divided into two regions, separated by a pivot point,  $X_{\text{pivot}}$ . This value determines the slope values:  $\alpha_{\text{BPL},1}$  for  $X \leq X_{\text{pivot}}$  and  $\alpha_{\text{BPL},2}$  for  $X > X_{\text{pivot}}$ . In the GDPL model, the transition between the slopes  $\alpha_{\text{GDPL},1}$  and  $\alpha_{\text{GDPL},2}$  is smoothed by a parameter  $\delta$ , that quantifies the width of the transition region between the slopes ([Pop et al. 2022a](#)).

The broken power law (BPL) model is defined as,

$$Y = A_{\text{BPL}} \cdot \begin{cases} \left( \frac{X}{X_{\text{pivot}}} \right)^{\alpha_{\text{BPL},1}} & X \leq X_{\text{pivot}} \\ \left( \frac{X}{X_{\text{pivot}}} \right)^{\alpha_{\text{BPL},2}} & X > X_{\text{pivot}} \end{cases} \quad (8)$$

The inclusion of a factor  $X_{\text{pivot}}^{-1}$  in the pieces ensures that they coincide at  $X = X_{\text{pivot}}$ , thereby guaranteeing continuity at that point.

The general double power law (GDPL) model is defined as,

$$Y = A_{\text{GDPL}} \left( \frac{X}{X_{\text{pivot}}} \right)^{\alpha_{\text{GDPL},1}} \left\{ \frac{1}{2} \left[ 1 + \left( \frac{X}{X_{\text{pivot}}} \right)^{\frac{1}{\delta}} \right] \right\}^{(\alpha_{\text{GDPL},2} - \alpha_{\text{GDPL},1})\delta} \quad (9)$$

The main advantage of the GDPL model over the SPL model is that it allows us to identify where self-similarity in the scaling relations holds. The  $X_{\text{pivot}}$  value defines the breakpoint between the first and second slopes, delineating the mass range where self-similarity breaks. While adding multiple slopes with several breakpoints could improve the model fitting performance, a single  $X_{\text{pivot}}$  with two slopes is sufficient to capture the effects of AGN feedback within the mass range of our sample, as shown in [P22](#).

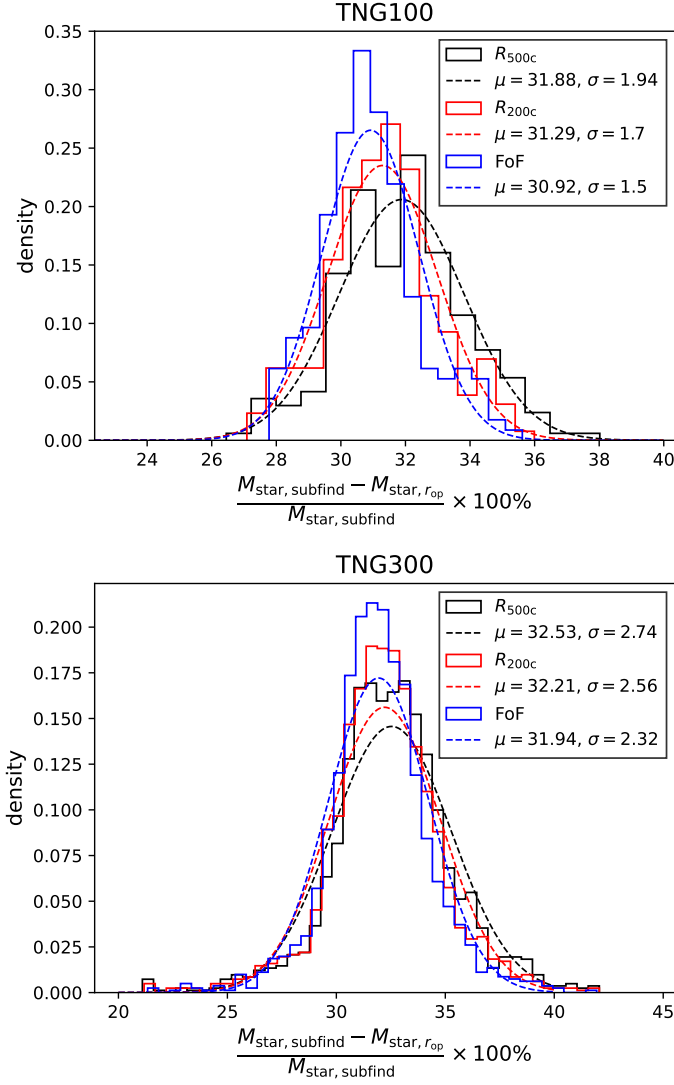


**Fig. 1.** Distribution of the percentage difference between the stellar masses from subfind and  $2 \times R_{M_{\text{star}}/2} \sim r_{\text{op}}$  apertures at different constraints: in an halocentric radius  $R_{500c}$  (black),  $R_{200c}$  (red), and the mass considered by the friends-of-friends (FoF) algorithm (blue). The dashed lines represent the normal distribution fitted in their respective constraint (and their respective color).

## 4. Results

### 4.1. Comparison between observations and IllustrisTNG

C18 measured halo masses using the SZ-effect, hot gas using the X-ray  $\beta$ -model, and the stellar mass of each galaxy through SED fitting and SMF construction, all within  $R_{500c}$ . Thus, we consider two measurements within the simulations:

- We took only the gas from the cluster with  $T \geq 10^7$  K enclosed within a sphere of radius  $R_{500c}$ . Regarding the stellar mass, it corresponds to the sum of the stellar masses of galaxies within a spherical aperture of twice the stellar half-mass radius ( $2 \times R_{M_{\text{star}}/2} \sim r_{\text{op}}$ ). Warm gas, cold gas, and the intra-cluster light (ICL) are not considered in this analysis.
- All gas and stars within the halo within a sphere of radius  $R_{500c}$ . This includes hot gas, warm gas, cold gas, galaxy stars, and the intracluster light (ICL).

The first approach is essential for comparing TNG100 and TNG300 with the observations from C18. The second helps examine the behaviour of the scaling relations when all components expected to be in the clusters are considered. We do not use the subfind aperture, as our goal is to create a measurement procedure as similar as possible to the observations and to characterize all baryonic components within the clusters. Fig. 1 shows the differences between the stellar masses defined by a subfind and a  $2 \times R_{M_{\text{star}}/2} \sim r_{\text{op}}$  apertures within  $R_{500c}$ ,  $R_{200c}$ , and FoF constraints regarding stellar masses. We find that the differences are approximately  $(31.88 \pm 1.94)$  per cent for TNG100 and  $(32.53 \pm 2.74)$  per cent for TNG300 within  $R_{500c}$ , comparable to those observed for other constraints. These differences are significant when calculating baryon fractions, fitting the SPL scaling relation, and comparing them with the scaling relations from C18. In the case of masses within  $R_{200c}$  and FoF, the percentages remain unchanged relative to  $R_{500c}$ , showing a tendency to range between 30.92% and 32.21% in both simulations.

Furthermore, we test the self-similarity of IllustrisTNG haloes. This aims to remove the redshift dependence from the baryon fraction, allowing us to fit a SPL that depends solely on the mass, as described by Eq. (6). We calculate the baryon fraction using Eq. (5) for haloes from TNG100 and TNG300 inside an  $R_{500}$  as described above. The SPL used in this case is the relation  $f_{\text{bar},500c} \propto (1+z)^{\alpha_{\text{SPL}}}$ . Fig. 2 shows the SPL fits of the IllustrisTNG haloes for the relation between baryon fraction and redshift, considering both comparison types. In the first type of comparison, the slopes of the SPL are  $\alpha_{\text{SPL}} \approx 0.029 \pm 0.051$  for TNG100 and  $\alpha_{\text{SPL}} \approx 0.071 \pm 0.021$  for TNG300. In the second type of comparison, the slopes are  $\alpha_{\text{SPL}} \approx 0.006 \pm 0.023$  for TNG100 and  $\alpha_{\text{SPL}} \approx 0.037 \pm 0.010$  for TNG300. These slopes were obtained using a non-linear least squares regression fit to our SPL model. The covariance matrix of the fit determines the slope errors. In the self-similar model presented by Kaiser (1986), the theoretical slope should be close to zero, as the baryonic matter should only scale with the total cluster mass, independently of redshift. Examining the slope values closely, all are positive, indicating a slight change in the scaling relations, with a minimal increase in the baryon fraction with redshift. However, the differences between the self-similar and simulation slopes are small, on the order of hundredths (and, in one case, thousandths). Thus, we confirm that the simulation slopes are effectively zero, removing the redshift dependence from the baryon fraction. Thus, the baryon fraction  $f_{\text{bar},500c}$  is expected to scale only with the mass  $M_{500c}$ .

Using the same baryon fractions, we perform an SPL fit for IllustrisTNG haloes to determine the slopes,  $\alpha_{\text{SPL}}$ , and compare them with the data from C18. The SPL used in this case is the relation  $f_{\text{bar},500c} \propto (M_{500c})^{\alpha_{\text{SPL}}}$ . Fig. 3 presents these results alongside the Universe's baryon fraction measured by Planck Collaboration et al. (2016a). The top panels clearly show that the observable data does not directly match TNG100 or TNG300. The reason for this discrepancy is that IllustrisTNG has an AGN feedback model that enriches efficiently the intra-cluster medium gas of the low massive clusters and the galaxy groups (Pop et al. 2022a). As a consequence, the fraction of baryons is raised at low mass values. However, this does not impact our analysis, as we focus on the behavior of the scaling relation. In this context, we find that in IllustrisTNG, the relations between the baryon fraction and halo mass yield a slope  $\alpha_{\text{SPL}} \approx 0.248 \pm 0.018$  for TNG100 and  $\alpha_{\text{SPL}} \approx 0.261 \pm 0.006$  for TNG300. Without considering redshift, C18 data provides an SPL scaling relation with a slope of  $\alpha_{\text{Chiu}} \approx 0.350 \pm 0.076$ . The scaling relations for TNG100, TNG300, and C18 data show similar behavior, with

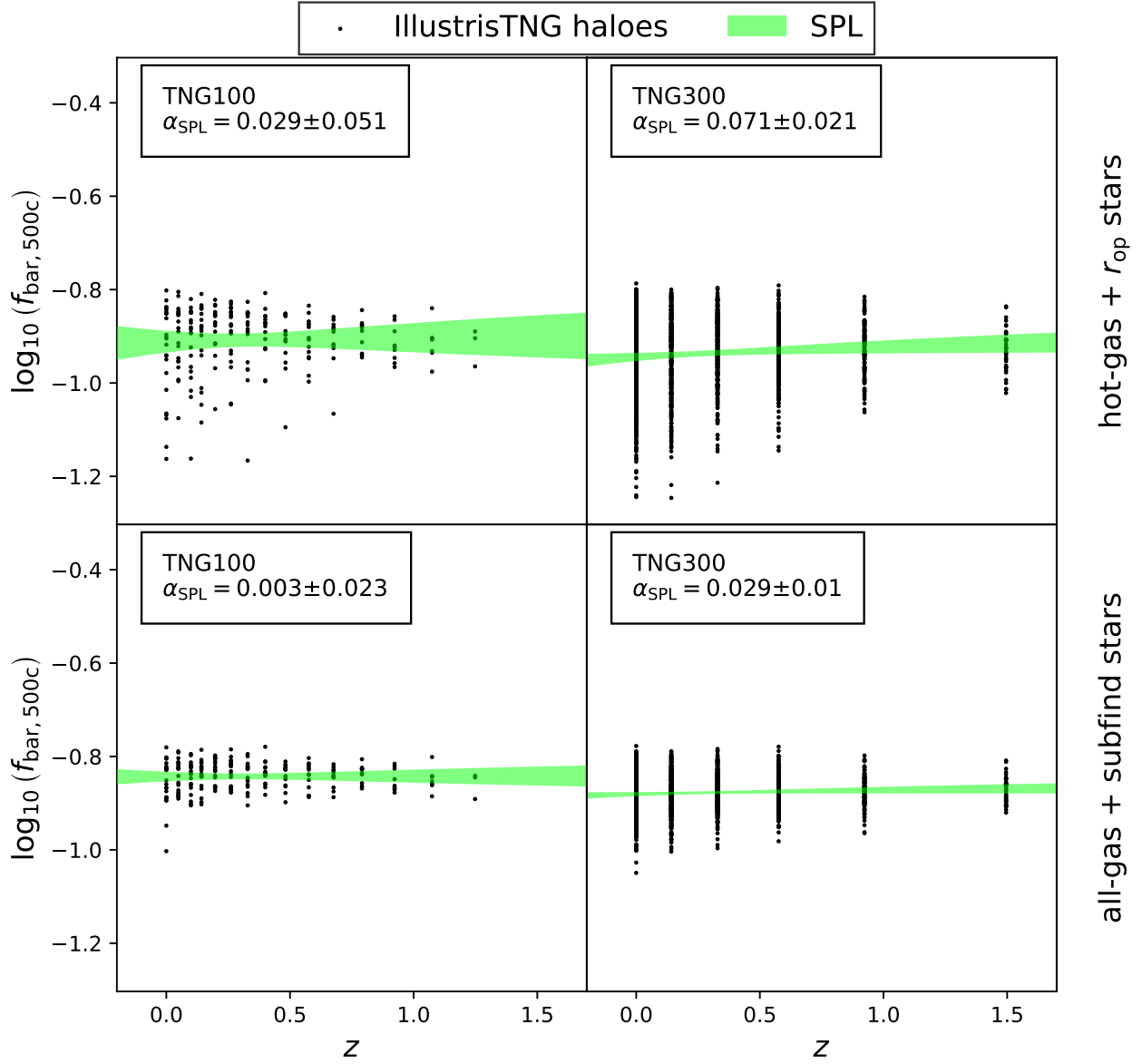


**Fig. 2.** The Simple Power Law (SPL) fit (green region) of the IllustrisTNG haloes (black dots), to the scaling relation of the mass fraction of baryons  $f_{\text{bar}}$ , in a radius  $R_{500c}$ , and the redshift  $z$ . All panels have their corresponding simulation name label and a value for the  $\alpha_{\text{SPL}}$  slope from the SPL fit in the upper-left corner. Top panels: The fraction of baryons includes the hot-gas and the  $2 \times R_{M_{\text{star}}/2} \sim r_{\text{op}}$  aperture. Bottom panels: The fraction of baryons includes all the gas and the subfind aperture. The shade areas are represented with a width of  $3\sigma$ .

baryon fractions increasing at high halo masses and decreasing at low halo masses. Furthermore, the slope values from IllustrisTNG and C18 agree within  $1 - 2\sigma$ . This agreement suggests that the IllustrisTNG results may provide insights into the missing baryons problem and help reconcile the tension with the hierarchical scenario highlighted by C18.

In the bottom panels of Fig (3), we show how the behavior of the scaling relations changes when the remaining gas ( $T < 10^7$  K) and all remaining stellar mass in the halo are included. At first glance, a direct comparison with C18 is not possible, as the parameters are not directly comparable. Although the general behavior remains, showing an increase in the baryon fraction, the slopes differ significantly between simulations and observations. We find a slope  $\alpha_{\text{SPL}} \simeq 0.071 \pm 0.010$  for TNG100 and  $\alpha_{\text{SPL}} \simeq 0.120 \pm 0.003$  for TNG300 in the scaling relations. These lower slopes arise from including the remaining gas and accounting for the ICL in the measurements, which

benefits low-mass haloes more than higher-mass ones. Consequently, low-mass haloes exhibit a greater fraction of cold gas compared to high-mass haloes (see Sections 4.2 and A). Additionally, more haloes in both simulations reach the universal fraction of baryon. Most haloes that fail to reach this value have masses of  $\log_{10}(M_{500c}/M_{\odot}) \lesssim 14$ . This mass threshold aligns with values reported in numerous studies discussing the breakdown of self-similarity in scaling relations (Pop et al. 2022a) and the redistribution of baryons in low-mass haloes by non-gravitational processes, such as AGN feedback (Ayromlou et al. 2023).

#### 4.2. Looking for the missing baryons

A limitation usually found in observations is the lack of information on the cold and warm gas components. As simulations

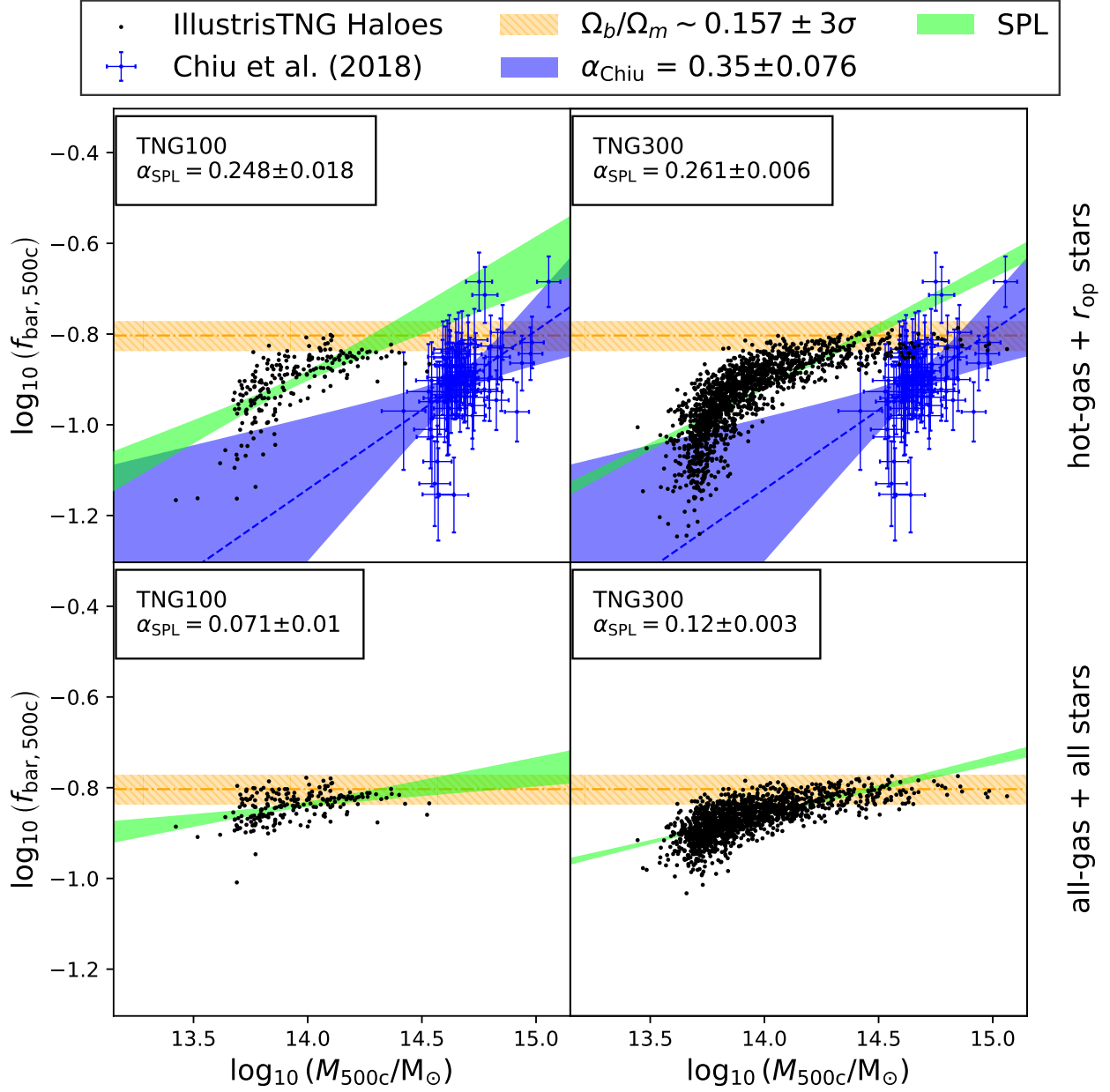


**Fig. 3.** The Simple Power Law (SPL) fit (green region) of the IllustrisTNG haloes (black dots), to the scaling relation of the mass fraction of baryons  $f_{\text{bar}}$  and halo mass  $M$  in a radius  $R_{500c}$ , for all redshifts. All panels have their respective simulation tag and a value for the  $\alpha_{\text{SPL}}$  slope from the SPL fit in the upper-left corner. Top panels: The fraction of baryons includes the hot-gas and the  $2 \times R_{M_{\text{star}}/2} \sim r_{\text{op}}$  aperture. Bottom panels: The fraction of baryons includes all the gas and all the stars inside the halo. The yellow areas represent the Planck Collaboration et al. (2016a) fraction of baryons. Also, the C18 data (blue dots) is shown with its SPL fit (blue areas). The shade areas are represented with a width of  $3\sigma$ .

do not have these issues, we will estimate which fraction of baryons we are undetecting when only considering the hot gas from the ICM. We divided the baryonic matter into cold gas, warm gas, and hot gas for the gaseous component; and into galaxy stellar mass (from  $r_{\text{op}}$  and subfind) and intra-cluster light (ICL) for the stellar component. Additionally, we split our clusters between low-mass  $\log_{10}(M_{500c}/M_{\odot}) < 14$  and high-mass haloes  $\log_{10}(M_{500c}/M_{\odot}) \geq 14$ . Our sample comprises 137 and 1115 low-mass haloes in IllustrisTNG-100 and IllustrisTNG-300, and 81 and 490 high-mass haloes in IllustrisTNG-100 and IllustrisTNG-300, respectively. Additionally, for visualization purposes, we include the complete sample (labeled as "all halo types") in the following figures.

Table 3 presents the baryonic mass fraction for each component in our clusters. The baryonic mass fraction is defined as the mass of each component ( $M_{\tau}$ ), divided by the total baryonic mass ( $M_{\text{bar}}$ ), where  $\tau = \{\text{cold gas, warm gas, hot gas, galaxy stars, ICL}\}$ . (see Appendix A and Figs. A.1) and A.2 for calculation and fitting details).

Additionally, Table 3 shows the average baryonic mass values for components not considered in C18 observations: cold gas, warm gas, and ICL ( $r_{\text{op}}$ ). The sum of those components is defined as the missing baryons from these simulations. The data in Table 3 reveal a tendency for low-mass haloes to contain more missing (undetected) baryons than high-mass haloes. Specifically, low-mass haloes exhibit approximately 17.83 per cent in TNG100 and 17.67 per cent in TNG300 of missing baryons. In



**Table 3.** Percentages of baryonic components.

Cluster type	Low mass haloes		High mass haloes		All haloes	
Mass threshold	$\log_{10}(M_{500c}/M_{\odot}) < 14$		$\log_{10}(M_{500c}/M_{\odot}) \geq 14$		All masses	
Simulation	TNG100	TNG300	TNG100	TNG300	TNG100	TNG300
% cold-gas	$1.66 \pm 0.12$	$1.08 \pm 0.03$	$0.60 \pm 0.07$	$0.34 \pm 0.02$	$1.27 \pm 0.09$	$0.86 \pm 0.03$
% warm-gas	$10.52 \pm 0.69$	$10.81 \pm 0.23$	$1.45 \pm 0.14$	$1.06 \pm 0.06$	$7.15 \pm 0.53$	$7.83 \pm 0.20$
% hot-gas	$70.95 \pm 0.79$	$74.87 \pm 0.26$	$82.92 \pm 0.30$	$88.45 \pm 0.12$	$75.39 \pm 0.64$	$79.01 \pm 0.24$
% galaxy stars ( $r_{\text{op}}$ )	$11.22 \pm 0.19$	$7.46 \pm 0.05$	$10.13 \pm 0.17$	$5.65 \pm 0.05$	$10.82 \pm 0.14$	$6.91 \pm 0.04$
% ICL ( $r_{\text{op}}$ )	$5.65 \pm 0.07$	$5.78 \pm 0.03$	$4.90 \pm 0.08$	$4.50 \pm 0.03$	$5.37 \pm 0.06$	$5.39 \pm 0.03$
% galaxy stars (subfind)	$16.50 \pm 0.26$	$11.04 \pm 0.07$	$14.75 \pm 0.23$	$8.36 \pm 0.07$	$15.85 \pm 0.19$	$10.22 \pm 0.06$
% ICL (subfind)	$0.46 \pm 0.02$	$1.79 \pm 0.02$	$0.31 \pm 0.02$	$1.64 \pm 0.03$	$0.40 \pm 0.02$	$1.69 \pm 0.02$
$\langle\%$ baryons "missed")	$\sim 17.83$	$\sim 17.67$	$\sim 6.95$	$\sim 5.90$	$\sim 13.79$	$\sim 14.08$

**Notes.** Percentages of the total baryonic mass in forms of cold-gas, warm-gas, hot-gas, galaxy star and ICL (both in  $r_{\text{op}}$  and subfind apertures) masses (see details of calculation in the Appendix A). Also, there is the ( $\%$  baryons "missed") value, which is calculate adding the percentage of cold-gas, warm-gas and ICL ( $r_{\text{op}}$ ) mean values. The standard error are explained in Appendix A.

contrast, high-mass haloes have about 6.95 per cent in TNG100 and 5.90 per cent in TNG300 of missing baryons. In both cases, hot gas remains the most significant baryonic component within the haloes. However, warm gas and ICL ( $r_{\text{op}}$ ) correspond to a non-negligible fraction of baryons "missed" in low-mass haloes. Conversely, most of the missing baryons are attributed to the ICL ( $r_{\text{op}}$ ) in high-mass haloes, which shows a similar proportional contribution to that observed in low-mass haloes. Finally, Table 3 also presents the stellar components measured using the subfind aperture, highlighting the differences between this method and the  $r_{\text{op}}$  aperture in terms of stellar mass measurements. The results show that the subfind algorithm collects more stellar mass within galaxies compared to the  $r_{\text{op}}$  spherical aperture. This is a consequence of the subfind algorithm, which, by construction, assigns to the central galaxy all particles within the virial radius that are not associated with any satellite subhalo (Springel et al. 2001; Dolag et al. 2009). As a result, diffuse stellar components, such as the stellar halo, are included as part of the central galaxy mass.

When considering all haloes, Table 3 shows that TNG100 and TNG300 have 13.79 per cent and 14.08 per cent of missing baryons respectively. The hot gas component remains the most significant baryonic component. The overall fractions are similar to those of low-mass haloes but with lower contributions from the warm gas and ICL ( $r_{\text{op}}$ ) components, as high-mass haloes are included in this analysis. Among all components, warm gas is the most affected when considering all haloes, showing a reduction of approximately 3 per cent compared to the low-mass haloes in both simulations. The ICL ( $r_{\text{op}}$ ) component also exhibits a reduction of about 0.40 per cent relative to the low-mass haloes in both simulations. This analysis highlights the importance of dividing the halo sample since baryons could be present in different states in high- and low-mass clusters.

Gouin et al. (2022) studied the distribution of gas components in TNG300 haloes at  $z = 0$ . These clusters were categorised by mass into clusters ( $M_{200c}/M_{\odot}/h > 1 \times 10^{14}$ ) and groups ( $5 \times 10^{13} < M_{200c}/M_{\odot}/h < 1 \times 10^{14}$ ) of galaxies. Additionally, they divided the gas into five independent phases: hot gas, warm dense gas (WCGM), warm diffuse gas (WHIM), cold dense gas (halo gas), and cold diffuse gas (IGM). They calculated the gas fraction of these phases as a function of  $R_{200}$ . Table 4 shows the relative gas percentages for our haloes, calculated based on the percentages in Table 3. Despite differences between our sample and the sample from Gouin et al. (2022), the gas fractions are remarkably similar at  $R \sim 0.6R_{200} \sim R_{500}$ . In galaxy

groups, most of the contribution to these percentages, besides the hot gas, comes from warm diffuse gas, which corresponds to the circumgalactic medium (CGM) (Gouin et al. 2022). At this radius, WCGM gas accounts for a larger fraction than WHIM gas. In galaxy clusters, the majority of the gas fraction comes from hot gas. Based on this analysis, the gas phase associated with the missing baryons in our sample is likely dominated by WCGM gas.

These results suggest that the break in the power-law seen in Fig. 3 are driven by the higher fractions of ICL, cold gas, and warm gas present in low-mass clusters compared to massive ones. Additionally, cold gas percentages are lower in all cases compared to warm gas. Therefore, the warm gas and the ICL in low-mass haloes are the primary contributors to the observed changes in baryonic scaling relations. This interpretation aligns with the WHIM proposal, which suggests that the missing baryons identified in C18 could reside in the warm diffuse phase. Furthermore, A23 propose that missing baryons are redistributed by non-gravitational processes (e.g., AGN, stellar, and UV feedback) into a region between  $1.5 - 2.5R_{200c}$ , where the baryon fraction reaches the universal value. Both scenarios are compatible, suggesting a coherent explanation for the missing baryons problem. This conclusion could have significant implications for future observational research related to the baryon distribution, mass measurements, and calibration of scaling relations.

#### 4.3. FoF masses in baryonic scaling relations

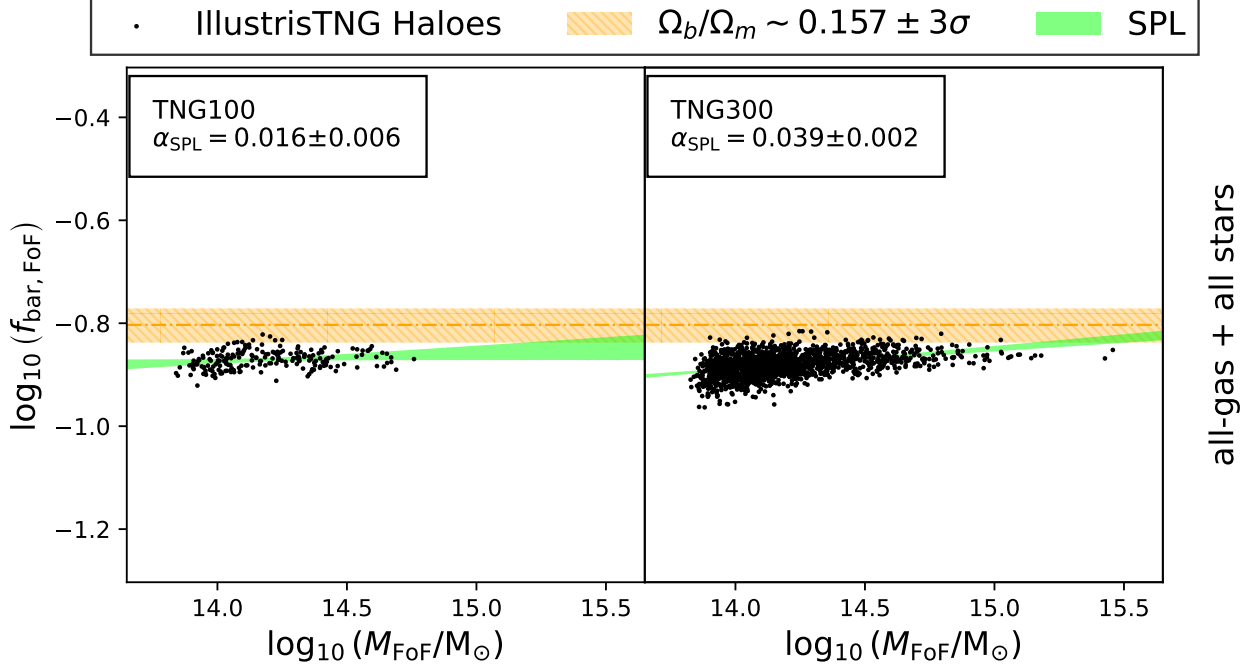
The changes in baryonic scaling relations when considering the total mass of haloes within a sphere radius  $R_{500c}$  are explored in Subsections 4.1 and 4.2. The  $R_{500c}$  is particularly useful for measuring gas masses, using X-ray and hot-the SZ effect in an observational context. In this section, we shift the mass variables from  $R_{500c}$  to masses defined by the FoF algorithm. i.e., accounting for all the mass "bound" to the cluster without a fixed aperture. This approach compares how scaling relations change when using these broader mass definitions.

Fig. 4 presents the SPL scaling relation models for baryonic mass fractions of IllustrisTNG haloes in the FoF delimited mass context. Comparing these results with the all-gas + all-stars scaling relations at  $R_{500c}$  shown in Fig. 3, we observe a mean slope difference of  $\alpha_{\text{SPL,FoF}} - \alpha_{\text{SPL},500c} \simeq -0.06$  in TNG100 and  $\alpha_{\text{SPL,FoF}} - \alpha_{\text{SPL},500c} \simeq 0.08$  in TNG300. In the FoF context, low-mass haloes boost their baryon fractions, displaying a tendency towards  $\alpha_{\text{SPL,FoF}} \rightarrow 0$  slopes in both simulations. This behav-



**Table 4.** Gas mass percentages.

Cluster type	Low mass haloes		High mass haloes		All haloes	
Mass threshold	$\log_{10}(M_{500c}/M_{\odot}) < 14$		$\log_{10}(M_{500c}/M_{\odot}) \geq 14$		All masses	
Simulation	TNG100	TNG300	TNG100	TNG300	TNG100	TNG300
% cold-gas	$2.00 \pm 0.15$	$1.25 \pm 0.04$	$0.71 \pm 0.08$	$0.38 \pm 0.02$	$1.52 \pm 0.11$	$0.98 \pm 0.04$
% warm-gas	$12.66 \pm 0.83$	$12.45 \pm 0.27$	$1.71 \pm 0.16$	$1.18 \pm 0.06$	$8.54 \pm 0.64$	$8.93 \pm 0.25$
% hot-gas	$85.34 \pm 0.95$	$86.29 \pm 0.30$	$97.57 \pm 0.36$	$98.42 \pm 0.40$	$89.94 \pm 0.65$	$89.95 \pm 0.27$

**Notes.** Percentages of the total gas mass component in form of cold-gas, warm-gas, hot-gas. These are calculated as the relative percentages, based in Table 3.

**Fig. 4.** The Simple Power Law (SPL) fit (green region) of the IllustrisTNG haloes (black dots), to the scaling relation of the mass fraction of baryons  $f_{\text{bar}}$  and halo mass  $M$  measured by friend-of-friends (FoF) algorithm, for all redshifts. All panels have their respective simulation tag and a value for the  $\alpha_{\text{SPL}}$  slope from the SPL fit in the upper-left corner. The fraction of baryons includes all the gas and all the stars inside the halo. The yellow region represent the Planck Collaboration et al. (2016a) fraction of baryons. All the regions are in  $3\sigma$ .

ior accounts for the differences observed with the  $R_{500c}$  mass context. Additionally, the self-similarity of the baryon fraction is satisfied, as the  $\alpha_{\text{SPL}, \text{FoF}} \rightarrow 0$  results are consistent with Eq. (6). Furthermore, these slope tendencies indicate that high-mass haloes can form through the assembly of low-mass haloes, reflecting the hierarchical formation scenario. However, most IllustrisTNG haloes fail to reach the baryon fraction measured by Planck Collaboration et al. (2016a) within the  $3\sigma_{\text{Planck}}$  region (with  $\sigma_{\text{Planck}} = 0.004$  being the error of the baryon fraction in Planck Collaboration et al. 2016a). Most haloes exhibit baryon fractions approximately 0.1 dex below the mean value, with only a few exceptions. This result suggests the re-emergence of the missing baryon problem in the FoF context, which will be further discussed in Section 5.

#### 4.4. Fitting power law models as scaling relations

In Fig. 3, we observe how the SPL model fits the scaling relations of baryon fractions in IllustrisTNG haloes. This provides a framework to compare the haloes with the scaling relations from C18. However, the distribution of scattered data and the SPL model's fit do not appear to align well. In the hot-gas +  $r_{\text{op}}$

star comparison, the data exhibit a knee-like shape with a break (or pivot) around the low- and high-mass halo limit. This feature arises due to AGN feedback, which redistributes baryons to the outskirts of low-mass haloes, reducing their baryon fractions and breaking self-similarity in these haloes (Ayromlou et al. 2023; Pop et al. 2022a). For this reason, the SPL model is insufficient for studying scaling relations across a wide range of haloes in the context of self-similarity (Pop et al. 2022a). To address this limitation, we require models capable of identifying the breakpoints in baryonic scaling relations, indicating where self-similarity is preserved. The models employed in this section are the BPL and GDPL models.

The method we follow is similar to that used by P22. We perform a non-linear least squares regression to fit the SPL, BPL, and GDPL models to the median baryon fraction values in the IllustrisTNG (TNG100 and TNG300) samples. To compute the median values, we use 20 bins. This is the same bins used by P22, but in a higher mass range ( $M_{500c} \in [10^{12} - 2 \times 10^{15}] M_{\odot}$ ). From these fits, we obtain the power-law parameters  $\alpha_{\text{SPL}}$ ,  $\alpha_{\text{BPL},1}$ ,  $\alpha_{\text{BPL},2}$ ,  $\alpha_{\text{GDPL},1}$ , and  $\alpha_{\text{GDPL},2}$ , along with the  $\delta$  and  $M_{\text{pivot}}$  parameters from the GDPL model (see details in Equations 7, 8,

and 9). The parameter  $M_{\text{pivot}}$  is a breakpoint, indicating whether self-similarity is maintained or broken.

Fig. 5 shows the SPL, BPL, and GDPL fits to the median values of the TNG100 and TNG300 halo samples, including the  $M_{\text{pivot}}$  value and the baryonic mass fraction of the Universe (Planck Collaboration et al. 2016a). All numerical values of the power-law parameters— $\alpha_{\text{SPL}}$ ,  $\alpha_{\text{BPL},1}$ ,  $\alpha_{\text{BPL},2}$ ,  $\alpha_{\text{GDPL},1}$ , and  $\alpha_{\text{GDPL},2}$ —as well as the GDPL smoothness parameter  $\delta$ , the  $M_{\text{pivot}}$  value, and the respective model  $\chi^2$ -test results are presented in Table 5. The mean values and their associated errors are obtained from the fits to the median values of the sample. To compute the  $\chi^2$ -test, we use the median values of the TNG100 and TNG300 halo samples along with the models fitted with their mean parameter values. As shown in Fig. 5, the BPL and GDPL models exhibit a shape closely matching the distribution of IllustrisTNG haloes in the hot-gas +  $r_{\text{op}}$  case. In contrast, the SPL model matches the distribution for intermediate masses well but overestimates the baryon fraction at both low- and high-mass extremes. In the all-gas + all-stars case, all three models demonstrate similar shapes compared to the halo median values, although the SPL model slightly overestimates the baryon fraction at the low- and high-mass extremes, albeit less prominently than in the hot-gas +  $r_{\text{op}}$  case. The  $\chi^2$ -test results for the SPL model support these claims, showing significant differences compared to the BPL and GDPL models in the hot-gas +  $r_{\text{op}}$  case, but no notable differences in the all-gas + all-stars case. As detailed in Table 5, the  $\chi^2$  values for the BPL and GDPL models are very close, with differences of  $\chi^2_{\text{GDPL}} - \chi^2_{\text{BPL}} \in [0, 0.001]$ , which is effectively negligible for both models.

In Table 5, we observe that the SPL parameter fits for TNG100 in both cases are closer to the parameters of the scaling relations in Fig. 3. However, the SPL parameter fits for TNG300 in both cases are less consistent with these scaling relation parameters. This discrepancy is not an issue, as a different fitting method is used in this analysis. Additionally, since both simulations use the same number of bins, TNG300 has a larger binning mass range than TNG100 due to the broader mass range of haloes in TNG300. We also find that the mean power-law parameters ( $\alpha$ ) for the BPL and GDPL models are identical. The differences lie in their standard deviation values, where the BPL model shows smaller deviations compared to the GDPL model. As seen in Fig. 5, these standard deviations are negligible within the IllustrisTNG halo mass range but become notable outside this range. This effect is more apparent in TNG100 than in TNG300, as the median mass values in TNG300 exhibit a flatter shape, leading the BPL and GDPL models to fit similarly. The  $M_{\text{pivot}}$  values in the BPL and GDPL models are identical, with a range of mean values  $\log_{10}(M_{\text{pivot}}/M_{\odot}) = 13.80 - 14.07$ . This range includes the  $\log_{10}(M_{500c}/M_{\odot}) \sim 14$  mass limit reported by P22 as the threshold for the loss of self-similarity in scaling relations, and by A23 as the upper limit for baryon redistribution driven by AGN feedback. This strongly suggests that AGN feedback lowers the baryonic mass fraction in low-mass haloes. Despite considering all baryonic components within  $R_{500c}$ , low-mass haloes still have reduced baryon fractions, while high-mass haloes approach the baryonic fraction value reported by Planck Collaboration et al. (2016a) within  $3\sigma_{\text{Planck}}$ . This supports the hypothesis that warm gas, cold gas, and ICL are underrepresented in observations. Finally, the mean softened transition parameter  $\delta$  for the GDPL models is consistent across both simulations and comparison types, with  $\delta \sim 0.25$ . The  $\sigma_{\delta}$  values are not significant, as  $\delta$  primarily governs the transition between  $\alpha_1$  and  $\alpha_2$ .

The BPL and GDPL scaling relations could significantly aid observations in characterizing non-gravitational processes using the baryon fraction of haloes, particularly in the context of galaxy clusters. The fact that IllustrisTNG matches the SPL model slopes derived by C18 establishes a solid framework for analyzing similar observations and comparing, for instance, slope results with simulations. In the observational domain, ongoing and future surveys such as the Dark Energy Survey (Collaboration: et al. 2016), Euclid (Laureijs et al. 2011), the Vera C. Rubin Observatory’s LSST (LSST Dark Energy Science Collaboration 2012), eROSITA (Merloni et al. 2012; Pillepich et al. 2012, 2018; Predehl et al. 2021; Bulbul et al. 2022), Athena X-ray observatory (Nandra et al. 2013), SPT-3G (Benson et al. 2014; Bender et al. 2018), CMB-S4 (Abazajian et al. 2016), CMB-HD (Sehgal et al. 2019), and Advanced ACTpol (Henderson et al. 2016) could validate and benefit from these models by comparing them with current and future cosmological hydrodynamical simulations. For instance, upcoming projects such as TNG-Cluster simulations (Nelson et al. 2024; Ayromlou et al. 2024; Lee et al. 2024; Lehle et al. 2024; Rohr et al. 2024; Truong et al. 2024), the MillenniumTNG Project (Hernández-Aguayo et al. 2023; Pakmor et al. 2023; Barrera et al. 2023; Kannan et al. 2023; Hadzhiyska et al. 2023; Hadzhiyska et al. 2023a,b; Bose et al. 2023; Contreras et al. 2023; Delgado et al. 2023; Ferlito et al. 2023), and the FLAMINGO simulations (Schaye et al. 2023; Kugel et al. 2023) could provide valuable insights. These simulations will also allow the extension of this framework by incorporating a larger sample of haloes, enabling a deeper understanding of baryonic scaling relations and their implications for cosmology.

## 5. Discussions

### 5.1. Mocks and the fraction of baryons

In an observational context, the measurement of masses is limited by the two-dimensional (2D) projection of the sky, which introduces biases in the estimates. Among the methods used to estimate mass, the Sunyaev-Zel’dovich (SZ) effect is useful for calculating  $M_{500c}$ , while X-ray  $\beta$ -model fitting is useful for calculating  $M_{\text{hot-gas},500c}$ . In contrast, simulations tend to overestimate observable values when using three-dimensional (3D) projections instead of 2D projections. Nevertheless, simulations can generate mocks that provide an estimate of the mean bias,  $b$ , between the mass computed in simulations,  $M_{500c}^{\text{SIM}}$ , and the observable mass in mocks,  $M_{500c}^{\text{EST}}$  (Pop et al. 2022b).

The relationship between these quantities is defined as,

$$b \equiv 1 - \frac{M_{500c}^{\text{EST}}}{M_{500c}^{\text{SIM}}}. \quad (10)$$

Pop et al. (2022b) studied the biases associated with the SZ effect,  $b_{\text{SZ}}$ , and X-ray techniques,  $b_X$ , in mass measurements using the MOCK-X pipeline in IllustrisTNG (Barnes et al. 2021). Pop et al. (2022b) identified 30,000 simulated galaxy groups and clusters with  $M_{500}$  ranging from  $10^{12}$  to  $2 \times 10^{15} M_{\odot}$  at  $z = 0$ . For haloes with  $M_{500} > 10^{13} M_{\odot}$ , the median hydrostatic mass bias was found to be  $b_{\text{SZ}} = 0.125 \pm 0.003$ , while the X-ray mass bias was  $b_X = 0.170 \pm 0.004$ .

If we consider both values for the estimation of the total mass  $M_{500c}$ , defined as  $M_{500c}^{\text{EST}} = (1 - b_i)M_{500c}^{\text{SIM}}$ , with  $b_i = \{b_X, b_{\text{SZ}}\}$ , we define  $f_{\text{bar},500c}^{\text{EST}} \equiv M_{\text{bar},500c}^{\text{EST}}/M_{500c}^{\text{EST}}$  as the synthetic baryon fraction, and  $f_{\text{bar},500c}^{\text{SIM}}$  as the simulated value. The relation between both

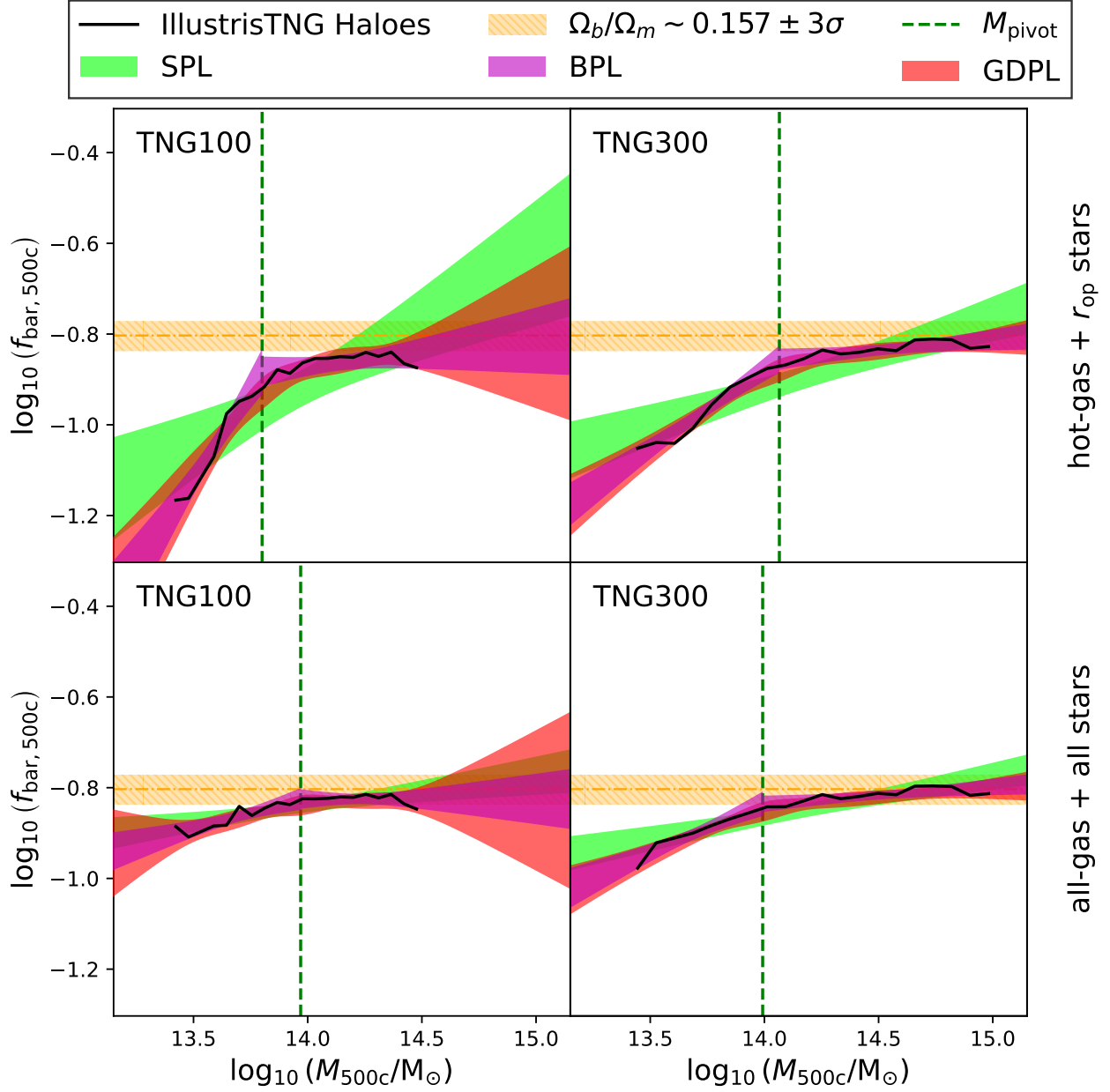


**Fig. 5.** The Simple Power Law (SPL) fit (green region), the Broken Power Law (BPL) fit (magenta region) and the General Double Power Law (GDPL) fit (red region) of the IllustrisTNG haloes (median of the data in black solid line), to the scaling relation of the mass fraction of baryons  $f_{\text{bar}}$  and halo mass  $M$  in a radius  $R_{500c}$ . All panels have their respective simulation tag in addition to a vertical dark green dashed line that represents the  $M_{\text{pivot}}$  of the broken fits. The power values of  $\alpha_{\text{SPL}}$  SPL fits,  $\alpha_{\text{BPL},1}$  and  $\alpha_{\text{BPL},2}$  BLP fits, and  $\alpha_{\text{GDPL},1}$  and  $\alpha_{\text{GDPL},2}$  GDPL fits, with the GDPL smoothness parameter  $\delta$  and  $M_{\text{pivot}}$  value are in the Table 5. (Top panels) The fraction of baryons includes the hot-gas and the  $2 \times R_{M_{\text{star}}/2} \sim r_{\text{op}}$  aperture. (Bottom panels) The fraction of baryons includes all the gas and all stars inside the halo. The yellow region represent the [Planck Collaboration et al. \(2016a\)](#) fraction of baryons. All the regions are in  $3\sigma$ .

baryon fractions can be written as  $f_{\text{bar},500c}^{\text{EST}} \equiv (1 - b_f)f_{\text{bar},500c}^{\text{SIM}}$ , where  $b_f$  is the baryon fraction bias. The parameter  $b_f$  can be related to  $b_i$ , and its associated uncertainty  $\sigma_{b_f}$ , through the following expressions,

$$b_f \equiv 1 - \frac{1}{1 - b_i} \quad (11)$$

$$\sigma_{b_f} = \frac{\sigma_{b_i}}{(1 - b_i)^2} \quad (12)$$

Using the values from [Pop et al. \(2022b\)](#), we find  $b_f \approx -0.1429 \pm 0.0039$  (for  $b_{\text{SZ}}$ ) and  $b_f \approx -0.2048 \pm 0.0058$  (for  $b_X$ ). Under these assumptions, we expect an overestimation in the baryon fraction from 14.29 to 20.48 per cent, which represents a significant departure from the results of [C18](#). However, this overestimation could be reduced if the baryonic mass bias  $b_{\text{bar}}$  could be estimated. A condition of  $b_{\text{bar}} > b_i$  would be required to produce a decrease in  $f_{\text{bar},500c}^{\text{EST}}$  relative to  $f_{\text{bar},500c}^{\text{SIM}}$ . Moreover,  $b_{\text{bar}}$  could account for individual biases associated with the stellar mass and the various gas phases.

**Table 5.** Fit values of SPL, BPL and GDPL models.

Comparison type	hot-gas and $r_{\text{op}}$ stars		all-gas and all stars	
Simulation	TNG100	TNG300	TNG100	TNG300
$\log_{10}(A_{\text{SPL}})$	$-4.70 \pm 0.60$	$-3.11 \pm 0.26$	$-1.79 \pm 0.18$	$-2.15 \pm 0.15$
$\alpha_{\text{SPL}}$	$0.27 \pm 0.04$	$0.16 \pm 0.02$	$0.07 \pm 0.01$	$0.09 \pm 0.01$
$\chi^2_{\text{SPL}}$	0.033	0.017	0.004	0.006
$\log_{10}(A_{\text{BPL}})$	$-0.88 \pm 0.01$	$-0.86 \pm 0.01$	$-0.82 \pm 0.01$	$-0.84 \pm 0.01$
$\alpha_{\text{BPL},1}$	$0.79 \pm 0.07$	$0.35 \pm 0.03$	$0.14 \pm 0.02$	$0.22 \pm 0.03$
$\alpha_{\text{BPL},2}$	$0.06 \pm 0.03$	$0.05 \pm 0.01$	$0.00 \pm 0.02$	$0.04 \pm 0.01$
$\chi^2_{\text{BPL}}$	0.004	0.002	0.002	0.001
$\log_{10}(A_{\text{GDPL}})$	$-0.93 \pm 0.01$	$-0.88 \pm 0.01$	$-0.84 \pm 0.01$	$-0.85 \pm 0.01$
$\alpha_{\text{GDPL},1}$	$0.79 \pm 0.12$	$0.35 \pm 0.04$	$0.14 \pm 0.09$	$0.22 \pm 0.04$
$\alpha_{\text{GDPL},2}$	$0.06 \pm 0.08$	$0.05 \pm 0.03$	$0.00 \pm 0.09$	$0.04 \pm 0.02$
$\delta$	$0.25 \pm 0.18$	$0.25 \pm 0.22$	$0.25 \pm 0.81$	$0.25 \pm 0.30$
$\chi^2_{\text{GDPL}}$	0.005	0.002	0.002	0.002
$\log_{10}(M_{\text{pivot}}/M_{\odot})$	$13.80 \pm 0.03$	$14.07 \pm 0.04$	$13.97 \pm 0.08$	$13.99 \pm 0.06$

**Notes.** Power values of  $\alpha_{\text{SPL}}$  SPL fits,  $\alpha_{\text{BPL},1}$  and  $\alpha_{\text{BPL},2}$  BPL fits, and  $\alpha_{\text{GDPL},1}$  and  $\alpha_{\text{GDPL},2}$  GDPL fits, with the GDPL smoothness parameter  $\delta$  and  $M_{\text{pivot}}$  value of Fig. 5. Also, it is included the  $\chi^2$  test of each models.

## 5.2. Mass accretion in FoF masses

The baryon fraction values derived from FoF in TNG100 and TNG300 differ from the Planck Collaboration et al. (2016a) value by approximately  $\sim 0.1$  dex, as shown in Fig. 4. This corresponds to  $f_{\text{TNG}}/(\Omega_b/\Omega_m) \simeq 0.79$ , indicating that about  $\sim 21$  per cent of baryons are missing within clusters compared to the universal value. The redistribution of baryons to the outskirts of haloes by AGN feedback could explain this discrepancy for low-mass clusters (Ayromlou et al. 2023). However, the issue persists at higher masses, where AGN feedback is insufficient to redistribute baryons to large distances. In this context, one might consider whether the relaxation state of clusters (relaxed or unrelaxed) contributes to this discrepancy. However, this seems unlikely, as the majority of haloes fall below the universal baryon fraction, regardless of their relaxation state.

It is worth noting that the FoF clustering algorithm assigns all particles gravitationally bound to the same halo. Because of this, this approach does not recover the universal baryon fraction, whereas methods using large concentric radii can achieve this at  $1.5 - 2.5R_{200c}$  (Ayromlou et al. 2023). The concentric radius method, however, introduces its own challenges. Specifically, it may include elements not gravitationally bound to the cluster and does not account for the cluster's shape, as it only considers elements within a sphere. It would be particularly interesting to investigate the relationship between the shape of galaxy clusters and their baryon fraction using the concentric radius method.

Returning to the FoF algorithm, the differences between the baryon fraction reported by Planck Collaboration et al. (2016a), and that of IllustrisTNG haloes could originate from two main explanations:

- The galaxy clusters are accreting dark matter efficiently.
- The galaxy clusters are accreting gas inefficiently.

Both hypotheses are related to the mass accretion rate (MAR) of dark matter ( $\text{MAR}_{\text{dm}}$ ) being higher than that of gas ( $\text{MAR}_{\text{gas}}$ ). Pizzardo et al. (2023b) developed a caustic technique to measure the mass accretion rate of galaxy clusters using spherical shells. The radii of these spherical shells are determined by the radial velocity profile, where the radial velocity satisfies  $v_{\text{rad}} \leq A \times v_{\text{min}}$ , with  $v_{\text{min}}$  being the minimum radial velocity in the cluster.  $A$  is an empirically determined adjustment parameter,

which is chosen to accurately capture the infall region described caustically. Pizzardo et al. (2023b) selected  $A = 0.72$  to have a  $r_{3c} = \text{MAR}_{3D}/\text{MAR}_c = 1.00 \pm 0.04$ , where  $\text{MAR}_{3D}$  and  $\text{MAR}_c$  are mass accretion rates obtained by 3D projections and by the caustic description respectively. Using TNG300, Pizzardo et al. (2023b) analyzed 1697 FoF haloes with  $M_{200c} \geq 10^{14} M_{\odot}$ , covering a redshift range of  $0.01 \leq z \leq 1.04$ , ultimately working with 1318 haloes. The remaining  $\sim 22$  per cent haloes were excluded due to limitations in the robust application of the caustic technique (Pizzardo et al. 2023a). An interesting result pertains to the mass accretion rates of galaxies and dark matter within these haloes. The study found that the  $\text{MAR}_{\text{dms}}$  are approximately 6.5 per cent lower than the galaxy mass accretion rates ( $\text{MAR}_{\text{galaxies}}$ ) (Pizzardo et al. 2023b). This discrepancy arises because the clustering amplitude of galaxies relative to dark matter is larger on smaller scales and at higher redshifts (Davis & Peebles 1983; Davis et al. 1985; Jenkins et al. 1998).

However, a challenge arises when attempting to apply this model to gas. This difficulty stems from the fact that IllustrisTNG employs a cell-based method to track the evolution of gas (Pillepich et al. 2018). With this approach, tracing the gas becomes challenging as its vectorial information is not retained. Consequently, a gas particle simulation suite is required for more accurate tracking. For instance, the FLAMINGO simulations (Schaye et al. 2023; Kugel et al. 2023) utilize a gas particle method in simulation boxes of 1.0 and 2.8 Gpc. The comparison of these results with FLAMINGO simulations, as well as the tracking of gas and its mass accretion rate, will be addressed in a future study.

## 6. Summary and conclusions

In this study, we examined the scaling relation differences between the state-of-the-art magnetohydrodynamic and cosmological simulations of IllustrisTNG and the 91 galaxy clusters identified via the SZ effect in the SPT-SZ survey (Bleem et al. 2015), as reported by C18. Our analysis focused on a simulation sample consisting of 218 haloes from TNG100 and 1604 haloes from TNG300, each with  $M_{200c} \geq 7 \times 10^{13} M_{\odot}$ . The baryonic mass fraction was defined as a function of halo mass within a concentric sphere of radius  $R_{500}$ , using the subfind algorithm to select galaxy components.



We defined two observational comparison cases: (1) incorporating only the hot gas in the halo and galaxy stars within a spherical aperture of  $2 \times R_{\text{star}/2} \sim r_{\text{op}}$ , and (2) including all baryonic components (gas and stars) in the halo, both analyzed at  $R_{500c}$ . To test the self-similarity of the haloes, we applied a SPL model and found that the slopes in both cases and simulations converge towards  $\alpha_{\text{SPL}} \rightarrow 0$ , indicating the elimination of redshift dependence in the scaling relations.

Our main findings can be summarized as follows:

- The slopes of the TNG100 and TNG300 haloes in the SPL scaling relations ( $\alpha_{\text{SPL}}$ ) align with the scaling relation slope values reported by C18 within error of  $1 - 2\sigma$  for the "hot-gas +  $r_{\text{op}}$  stars" case. This suggests a potential solution to the missing baryons problem identified in C18 and the tensions within the hierarchical formation scenario.
- When including all baryonic components (hot-gas, warm-gas, cold-gas, ICL, galaxy stars), the SPL scaling relations exhibit a null slope. Low-mass haloes ( $\log_{10}(M_{500c}/M_{\odot}) \lesssim 14$ ) show significantly elevated baryonic fractions but do not reach the universal baryon fraction, whereas high-mass haloes ( $\log_{10}(M_{500c}/M_{\odot}) \gtrsim 14$ ) achieve this value. This mass threshold correlates with the loss of self-similarity in the haloes and suggests that non-gravitational processes play a critical role in baryon redistribution.
- The mean percentage of missing baryons is notably higher in low-mass haloes ( $\sim 17.67$  per cent in TNG100, and  $\sim 17.80$  per cent in TNG300) compared to high-mass haloes ( $\sim 6.95$  per cent in TNG100, and  $\sim 5.90$  per cent in TNG300). This disparity accounts for the observed behavioral differences in scaling relations across different baryonic component configurations. Furthermore, the missing baryons in the IllustrisTNG haloes are primarily due to the exclusion of ICL and warm gas, particularly in low-mass haloes, while cold gas does not significantly contribute to the total missing components. This observation strongly supports the warm-hot intergalactic medium (WHIM) scenario.
- Our analysis indicates that the discrepancies in galaxy apertures, particularly in the characterization of ICL, can result in a significant variation of approximately 5 per cent in the percentage of missing baryons, depending on the method used to measure stellar mass. This variability must be considered in observational studies.

We discussed the accretion of baryonic components within FoF haloes, highlighting that approximately  $\sim 21$  per cent of baryons are missing compared to the expected universal fraction (Planck Collaboration et al. 2016a). While the redistribution of baryons to the outskirts of low-mass haloes (Gouin et al. 2022; Ayromlou et al. 2023) may account for this deficit, it does not explain the missing baryons in high-mass haloes. We hypothesize that FoF haloes may either be efficiently accreting dark matter or inefficiently accreting gas. Although the dark matter mass accretion rate ( $\text{MAR}_{\text{dm}}$ ) can be traced in IllustrisTNG using a caustic technique (Pizzardo et al. 2023b,a), the gas mass accretion rate ( $\text{MAR}_{\text{gas}}$ ) cannot be similarly traced due to the absence of positional and vectorial information for gas cells in IllustrisTNG. Future work will focus on following the gas particle of SPH simulation suites, such as FLAMINGO, to track gas accretion more effectively and calculate  $\text{MAR}_{\text{gas}}$ .

Finally, we emphasized the importance of incorporating non-gravitational processes into scaling relation analyses, particularly through the BPL and GDPL models. These models allowed us to identify critical mass break points where self-similarity is

either lost or preserved. Future observational surveys could validate and refine these models, especially when compared with current and upcoming simulations of large haloes. Such efforts may expand this framework by integrating additional data, further improving our understanding of baryonic scaling relations and their implications for cosmology.

**Acknowledgements.** We thank the EVOLGAL4D Computational Galaxy Formation and Evolution team of Pontificia Universidad Católica de Chile for the support during all the research time (visit EVOLGAL4D website in <https://www.evolgal4d.com/>). We thank Facundo Gómez and Joseph J. Mohr for the early discussions about this topic. We thank the anonymous referee for their constructive comments and suggestions, which helped improve the clarity and quality of this manuscript. This work was supported by partial funding from the ANID Basal Project FB210003. DM acknowledges financial support from PUCV Maintenance and Tuition Grants. DP acknowledges financial support from ANID through FONDECYT Postdoctorado Project 3230379. DP also gratefully acknowledges financial support from ANID - MILENIO - NCN2024\_112. PBT acknowledges the partial funding by FONDECYT 1240465. This research made use of several software packages, including NumPy (Harris et al. 2020), SciPy (Virtanen et al. 2020), Pandas (McKinney 2010), and all figures were generated using matplotlib (Hunter 2007).

## Data availability

The data from the IllustrisTNG simulations used in this work is publicly available on the IllustrisTNG website (<https://www.tng-project.org/>). The haloes were selected using the JupyterLab Workspace and their own IllustrisTNG modules. The data of the SPT-SZ survey clusters is available in tables (1) and (2) of C18 work.

## References

- Abazajian, K. N., Adshead, P., Ahmed, Z., et al. 2016, arXiv e-prints, [arXiv:1610.02743]
- Arnaud, M. & Evrard, A. E. 1999, MNRAS, 305, 631
- Arnaud, M., Pointecouteau, E., & Pratt, G. W. 2007, A&A, 474, L37
- Ayromlou, M., Nelson, D., & Pillepich, A. 2023, MNRAS, 524, 5391
- Ayromlou, M., Nelson, D., Pillepich, A., et al. 2024, A&A, 690, A20
- Ayromlou, M., Nelson, D., Yates, R. M., et al. 2021, MNRAS, 502, 1051
- Barnes, D. J., Vogelsberger, M., Pearce, F. A., et al. 2021, MNRAS, 506, 2533
- Barrera, M., Springel, V., White, S. D. M., et al. 2023, MNRAS, 525, 6312
- Bender, A. N., Ade, P. A. R., Ahmed, Z., et al. 2018, in Proc. SPIE, ed. J. Zmuidzinas & J.-R. Gao, Vol. 10708, 1070803
- Benson, B. A., Ade, P. A. R., Ahmed, Z., et al. 2014, in Proc. SPIE, ed. W. S. Holland & J. Zmuidzinas, Vol. 9153, 91531P
- Bleem, L. E., Stalder, B., de Haan, T., et al. 2015, ApJS, 216, 27
- Bocquet, S., Saro, A., Mohr, J. J., et al. 2015, ApJ, 799, 214
- Bose, S., Hadzhiyska, B., Barrera, M., et al. 2023, MNRAS, 524, 2579
- Bryan, G. L. & Norman, M. L. 1998, ApJ, 495, 80
- Bulbul, E., Liu, A., Pasini, T., et al. 2022, A&A, 661, A10
- Carlstrom, J. E., Holder, G. P., & Reese, E. D. 2002, ARA&A, 40, 643
- Cen, R. & Ostriker, J. P. 1999, ApJ, 514, 1
- Chiu, I., Mohr, J. J., McDonald, M., et al. 2018, MNRAS, 478, 3072
- Collaboration, D. E. S., Abbott, T., Abdalla, F. B., et al. 2016, MNRAS, 460, 1270
- Contreras, S., Angulo, R. E., Springel, V., et al. 2023, MNRAS, 524, 2489
- Dark Energy Survey Collaboration, Abbott, T., Abdalla, F. B., et al. 2016, MNRAS, 460, 1270
- Davis, M. & Djorgovski, S. 1985, ApJ, 299, 15
- Davis, M., Efstathiou, G., Frenk, C. S., & White, S. D. M. 1985, ApJ, 292, 371
- Davis, M. & Peebles, P. J. E. 1983, ApJ, 267, 465
- de Graaff, A., Cai, Y.-C., Heymans, C., & Peacock, J. A. 2019, A&A, 624, A48
- de Haan, T., Benson, B. A., Bleem, L. E., et al. 2016, ApJ, 832, 95
- Delgado, A. M., Hadzhiyska, B., Bose, S., et al. 2023, MNRAS, 523, 5899
- Dolag, K., Borgani, S., Murante, G., & Springel, V. 2009, MNRAS, 399, 497
- Drinkwater, M. J., Gregg, M. D., & Colless, M. 2001, ApJ, 548, L139
- Ettori, S. 2003, MNRAS, 344, L13
- Evrard, A. E. 1997, MNRAS, 292, 289
- Fabjan, D., Borgani, S., Rasia, E., et al. 2011, MNRAS, 416, 801
- Fazio, G. G., Hora, J. L., Allen, L. E., et al. 2004, ApJS, 154, 10
- Ferlito, F., Springel, V., Davies, C. T., et al. 2023, MNRAS, 524, 5591
- Giodini, S., Pierini, D., Finoguenov, A., et al. 2009, ApJ, 703, 982

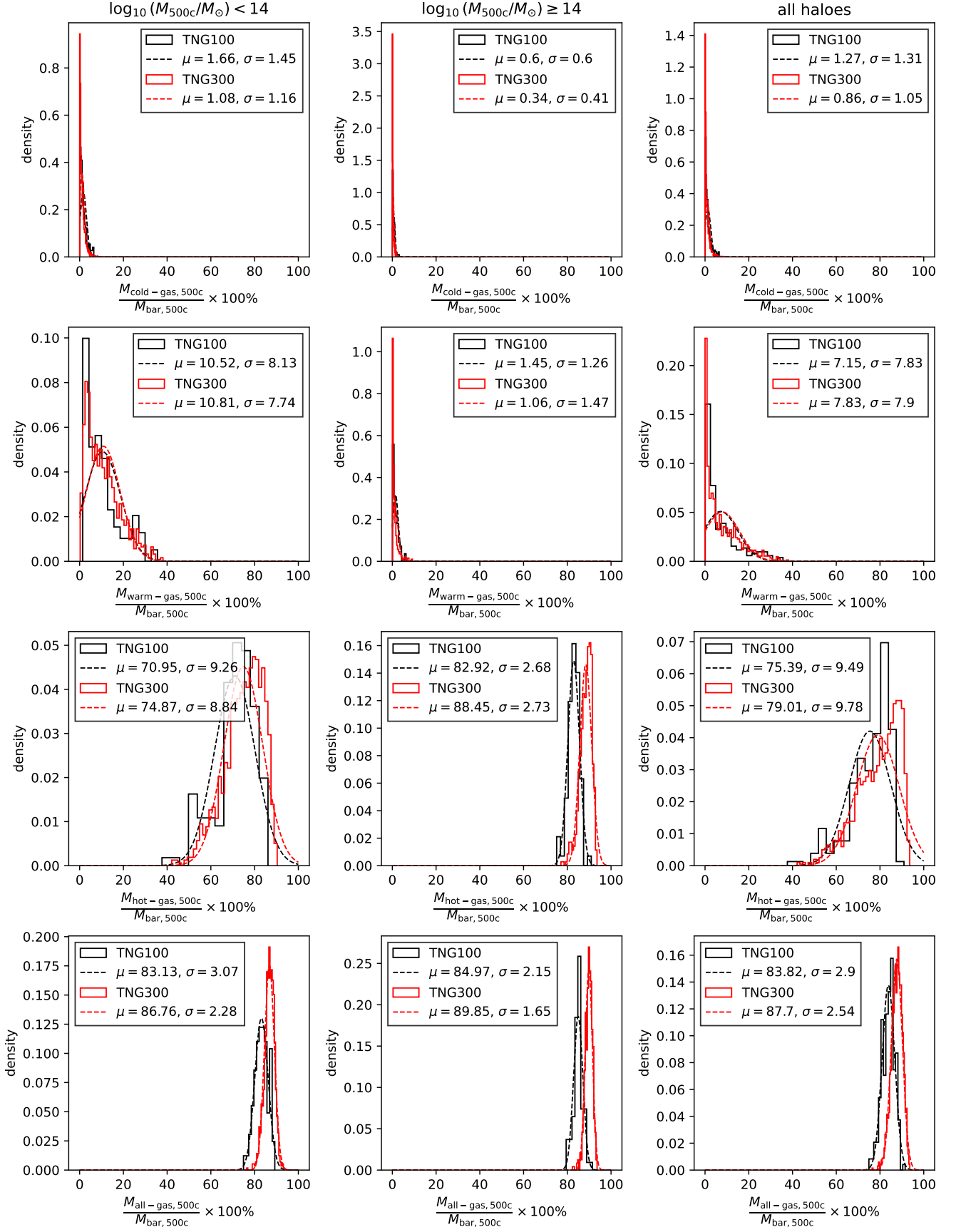
- Gouin, C., Bonamente, M., Galárraga-Espinosa, D., Walker, S., & Mirakhor, M. 2023, A&A, 680, A94
- Gouin, C., Gallo, S., & Aghanim, N. 2022, A&A, 664, A198
- Hadzhiyska, B., Eisenstein, D., Hernquist, L., et al. 2023, MNRAS, 524, 2507
- Hadzhiyska, B., Ferraro, S., Pakmor, R., et al. 2023a, MNRAS, 526, 369
- Hadzhiyska, B., Hernquist, L., Eisenstein, D., et al. 2023b, MNRAS, 524, 2524
- Haider, M., Steinhäuser, D., Vogelsberger, M., et al. 2016, MNRAS, 457, 3024
- Haiman, Z., Mohr, J. J., & Holder, G. P. 2001, ApJ, 553, 545
- Harris, C. R., Millman, K. J., van der Walt, S. J., et al. 2020, Nature, 585, 357
- Henden, N. A., Puchwein, E., Shen, S., & Sijacki, D. 2018, MNRAS, 479, 5385
- Henden, N. A., Puchwein, E., & Sijacki, D. 2019, MNRAS, 489, 2439
- Henderson, S. W., Allison, R., Austermann, J., et al. 2016, J. Low Temp. Phys., 184, 772
- Hernández-Aguayo, C., Springel, V., Pakmor, R., et al. 2023, MNRAS, 524, 2556
- Holder, G., Haiman, Z., & Mohr, J. J. 2001, ApJ, 560, L111
- Hunter, J. D. 2007, Comp. Sci. Eng., 9, 90
- Jenkins, A., Frenk, C. S., Pearce, F. R., et al. 1998, ApJ, 499, 20
- Jóhannesson, G., Björnsson, G., & Gudmundsson, E. H. 2006, ApJ, 640, L5
- Johnson, S. D., Mulchaey, J. S., Chen, H.-W., et al. 2019, ApJ, 884, L31
- Kaiser, N. 1986, MNRAS, 222, 323
- Kannan, R., Springel, V., Hernquist, L., et al. 2023, MNRAS, 524, 2594
- Kugel, R., Schaye, J., Schaller, M., et al. 2023, MNRAS, 526, 6103
- Laureijs, R., Amiaux, J., Arduini, S., et al. 2011, arXiv e-prints, [arXiv:1110.3193]
- Le Brun, A. M. C., McCarthy, I. G., Schaye, J., & Ponman, T. J. 2016, MNRAS, 466, 4442
- Lee, W., Pillepich, A., ZuHone, J., et al. 2024, A&A, 686, A55
- Lehle, K., Nelson, D., Pillepich, A., Truong, N., & Rohr, E. 2024, A&A, 687, A129
- Lim, S. H., Barnes, D., Vogelsberger, M., et al. 2021, MNRAS, 504, 5131
- Lotka, A. J. 1926, J. Wash. Acad. Sci., 16, 317
- Lovisari, L., Reiprich, T. H., & Schellenberger, G. 2015, A&A, 573, A118
- LSST Dark Energy Science Collaboration. 2012, arXiv e-prints, [arXiv:1211.0310]
- Mantz, A. B., Allen, S. W., Morris, R. G., et al. 2016, MNRAS, 463, 3582
- Marinacci, F., Vogelsberger, M., Pakmor, R., et al. 2018, MNRAS, 480, 5113
- Martizzi, D., Vogelsberger, M., Artale, M. C., et al. 2019, MNRAS, 486, 3766
- McDonald, M., Benson, B. A., Vikhlinin, A., et al. 2013, ApJ, 774, 23
- McGaugh, S. S., Schombert, J. M., de Blok, W. J. G., & Zagursky, M. J. 2010, ApJ, 708, L14
- McGee, S. L., Balogh, M. L., Bower, R. G., Font, A. S., & McCarthy, I. G. 2009, MNRAS, 400, 937
- McKinney, W. 2010, in Proc. 9th Python in Science Conference, ed. S. van der Walt & J. Millman, 56–61
- Merloni, A., Predehl, P., Becker, W., et al. 2012, arXiv e-prints, [arXiv:1209.3114]
- Mohr, J. J. & Evrard, A. E. 1997, ApJ, 491, 38
- Mohr, J. J., Mathiesen, B., & Evrard, A. E. 1999, ApJ, 517, 627
- Mulroy, S. L., Farahi, A., Evrard, A. E., et al. 2019, MNRAS, 484, 60
- Nagai, D., Kravtsov, A. V., & Vikhlinin, A. 2007, ApJ, 668, 1
- Naiman, J. P., Pillepich, A., Springel, V., et al. 2018, MNRAS, 477, 1206
- Nandra, K., Barret, D., Barcons, X., et al. 2013, arXiv e-prints, [arXiv:1306.2307]
- Nelson, D., Pillepich, A., Ayromlou, M., et al. 2024, A&A, 686, A157
- Nelson, D., Pillepich, A., Springel, V., et al. 2018, MNRAS, 475, 624
- Nicastro, F., Fang, T., & Mathur, S. 2022, arXiv e-prints, [arXiv:2203.15666]
- Nicastro, F., Kaastra, J., Krongold, Y., et al. 2018, Nature, 558, 406
- O’Hara, T. B., Mohr, J. J., Bialek, J. J., & Evrard, A. E. 2006, ApJ, 639, 64
- Pakmor, R., Bauer, A., & Springel, V. 2011, MNRAS, 418, 1392
- Pakmor, R. & Springel, V. 2013, MNRAS, 432, 176
- Pakmor, R., Springel, V., Coles, J. P., et al. 2023, MNRAS, 524, 2539
- Pallero, D., Gómez, F. A., Padilla, N. D., et al. 2019, MNRAS, 488, 847
- Pike, S. R., Kay, S. T., Newton, R. D. A., Thomas, P. A., & Jenkins, A. 2014, MNRAS, 445, 1774
- Pillepich, A., Nelson, D., Hernquist, L., et al. 2018, MNRAS, 475, 648
- Pillepich, A., Porciani, C., & Reiprich, T. H. 2012, MNRAS, 422, 44
- Pillepich, A., Reiprich, T. H., Porciani, C., Borm, K., & Merloni, A. 2018, MNRAS, 481, 613
- Pillepich, A., Springel, V., Nelson, D., et al. 2018, MNRAS, 473, 4077
- Pizzardo, M., Geller, M. J., Kenyon, S. J., Damjanov, I., & Diaferio, A. 2023a, A&A, 675, A56
- Pizzardo, M., Geller, M. J., Kenyon, S. J., Damjanov, I., & Diaferio, A. 2023b, A&A, 680, A48
- Planck Collaboration, Ade, P. A. R., Aghanim, N., et al. 2016a, A&A, 594, A13
- Planck Collaboration, Aghanim, N., Arnaud, M., et al. 2016b, A&A, 594, A22
- Planck Collaboration, Borgani, S., Fabjan, D., et al. 2013, MNRAS, 438, 195
- Pop, A.-R., Hernquist, L., Nagai, D., et al. 2022a, MNRAS, submitted [arXiv:2205.11528]
- Pop, A.-R., Hernquist, L., Nagai, D., et al. 2022b, MNRAS, submitted [arXiv:2205.11537]
- Pratt, G. W., Croston, J. H., Arnaud, M., & Böhringer, H. 2009, A&A, 498, 361
- Predehl, P., Andritschke, R., Arefiev, V., et al. 2021, A&A, 647, A1
- Press, W. H. & Schechter, P. 1974, ApJ, 187, 425
- Puchwein, E., Sijacki, D., & Springel, V. 2008, ApJ, 687, L53
- Reiprich, T. H. & Böhringer, H. 2002, ApJ, 567, 716
- Rohr, E., Pillepich, A., Nelson, D., Ayromlou, M., & Zinger, E. 2024, A&A, 686, A86
- Sanderson, A. J. R., O’Sullivan, E., Ponman, T. J., et al. 2013, MNRAS, 429, 3288
- Schaye, J., Kugel, R., Schaller, M., et al. 2023, MNRAS, 526, 4978
- Schechter, P. 1976, ApJ, 203, 297
- Sehgal, N., Aiola, S., Akrami, Y., et al. 2019, in BAAS, Vol. 51, 6
- Shull, J. M., Smith, B. D., & Danforth, C. W. 2012, ApJ, 759, 23
- Springel, V. 2010, MNRAS, 401, 791
- Springel, V., Pakmor, R., Pillepich, A., et al. 2018, MNRAS, 475, 676
- Springel, V., White, S. D. M., Tormen, G., & Kauffmann, G. 2001, MNRAS, 328, 726
- Stanek, R., Rasia, E., Evrard, A. E., Pearce, F., & Gazzola, L. 2010, ApJ, 715, 1508
- Sun, M., Voit, G. M., Donahue, M., et al. 2009, ApJ, 693, 1142
- Sunyaev, R. A. & Zeldovich, Y. B. 1972, Comments Astrophys. Space Phys., 4, 173
- Truong, N., Pillepich, A., Nelson, D., et al. 2024, A&A, 686, A200
- Truong, N., Rasia, E., Mazzotta, P., et al. 2017, MNRAS, 474, 4089
- Vikhlinin, A., Burenin, R. A., Ebeling, H., et al. 2009, ApJ, 692, 1033
- Villumsen, J. V. 1982, MNRAS, 199, 493
- Virtanen, P., Gommers, R., Oliphant, T. E., et al. 2020, Nat. Methods, 17, 261
- Walker, S., Simionescu, A., Nagai, D., et al. 2019, Space Sci. Rev., 215, 7
- Weinberger, R., Springel, V., Hernquist, L., et al. 2017, MNRAS, 465, 3291
- White, S. D. M. 1978, MNRAS, 184, 185
- White, S. D. M. & Frenk, C. S. 1991, ApJ, 379, 52
- White, S. D. M. & Rees, M. J. 1978, MNRAS, 183, 341
- Wright, E. L., Eisenhardt, P. R. M., Mainzer, A. K., et al. 2010, AJ, 140, 1868
- Yang, T., Cai, Y.-C., Cui, W., et al. 2022, MNRAS, 516, 4084

## Appendix A: Calculating baryonic component percentages

The baryonic component percentages are calculated by a fitting of a normal distribution, given by the Eq. (A.1), where the baryonic X percentage is given by  $\%M_{X,\text{bar}} \equiv (M_{X,\text{bar}}/M_{\text{bar}}) \times 100$  per cent, with  $M_{X,\text{bar}}$  the baryonic X component mass and  $M_{\text{bar}}$  the total baryonic mass of the cluster. Also  $\mu$  is the mean baryonic percentage value and  $\sigma$  is the standard deviation of it.

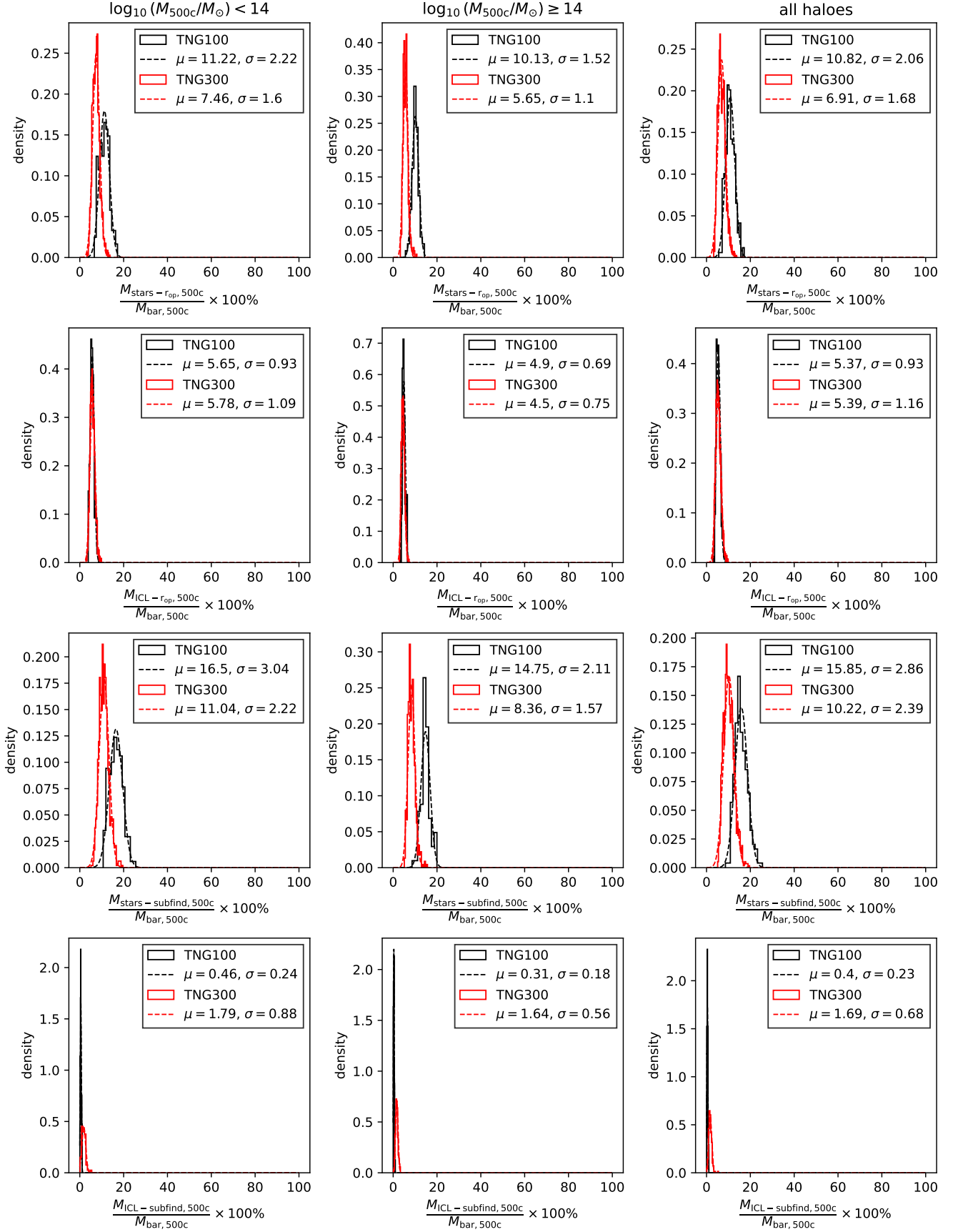
$$f(\%M_{X,\text{bar}}) = \frac{1}{\sqrt{2\pi}\sigma} e^{-\frac{(\%M_{X,\text{bar}} - \mu)^2}{2\sigma^2}} \quad (\text{A.1})$$

Fig. A.1 shows the distributions of the gas component percentages (cold, warm, and hot), while Fig. A.2 illustrates the distributions of the stellar component percentages (galaxies and ICL, using  $r_{\text{op}}$  and subfind apertures). In this context, comparing these percentages with the total baryonic mass of the clusters is crucial, as it provides a straightforward way to analyze the scatter in TNG100 and TNG300 haloes. For instance, low-mass haloes exhibit a high scatter in the hot gas percentages, which consequently results in a high scatter across all haloes for this component. A similar trend is observed for warm and cold gas components, where the standard deviation is comparable to the mean values. This occurs due to the significant number of clusters with low percentages for these components, which affects the shape of the distribution. Nevertheless, there are numerous clusters with high warm and cold gas percentages, supporting the inclusion of these components as "missing baryons" within the simulation environment. Additionally, the standard error, calculated as  $\sigma/\sqrt{N}$  (where  $N$  is the sample size), is on the order of tenths (see Table 3), making these percentages comparable to each other. Another baryonic component identified as missing is the ICL, which is derived from the difference between the stellar halo and the galaxies within the halo. The differences between  $r_{\text{op}}$  and subfind apertures are evident, with the latter capturing most of the stellar components of the haloes (see Section 4.1 and Fig. 1) for details.



**Fig. A.1.** Percentage distributions of cold-gas ( $T < 10^5$  K in upper row panels), warm-gas ( $10^5 \leq T < 10^7$  K in upper-center row panels), hot-gas ( $T \geq 10^7$  K in bottom-center row panels) and all-gas (in bottom row panels) masses considering the baryonic masses. The histograms are divided in the haloes with  $\log_{10}(M_{500c}/M_{\odot}) < 14$  (left column panels),  $\log_{10}(M_{500c}/M_{\odot}) \geq 14$  (center column panels) and all halo (right column panels) masses. (Black histograms) TNG100 haloes. (Red histograms) TNG300 haloes. The dashed lines represent the normal distribution fitted in their respective histogram (with their respective color).





**Fig. A.2.** Percentual distributions stellar masses considering the baryonic masses. Stellar galaxy mass in  $r_{\text{op}}$  aperture (upper row panels), ICL mass in  $r_{\text{op}}$  aperture (upper center row panels), stellar galaxy mass in subfind aperture (bottom center row panels) and ICL mass in subfind aperture (bottom row panels). The histograms are divided in the haloes with  $\log_{10}(M_{500c}/M_{\odot}) < 14$  (left column panels),  $\log_{10}(M_{500c}/M_{\odot}) \geq 14$  (center column panels) and all halo (right column panels) masses. (Black histograms) TNG100 haloes. (Red histograms) TNG300 haloes. The dashed lines represent the normal distribution fitted in their respective histogram (with their respective color).